REPORT DOCUMENTATION PAGE

Form Approved
OMB No. 0704-0188

1. REPORT DATE	2. REPORT TYPE	3. DATES COVERED
6/30/2016	Final	7 Aug 2015 - 31 May 2016

4. TITLE AND SUBTITLE
A Structural Biology and Protein Engineering Approach to the Engineering highly proficient catalytic bioscavengers for in vivo detoxification of a broad spectrum of nerve agents

5a. CONTRACT NUMBER
HDTRA1-11-C-0026

5b. GRANT NUMBER

5c. PROGRAM ELEMENT NUMBER

6. AUTHOR(S)
Dan S. Tawfik - PI
Joel L. Sussman - Co PI
David Baker - Co PI

E-Mail: Dan.Tawfik@weizmann.ac.il

5d. PROJECT NUMBER

5e. TASK NUMBER

5f. WORK UNIT NUMBER

7. PERFORMING ORGANIZATION NAME(S) AND ADDRESS(ES)
Weizmann Institute of Science
Rehovot 76100 ISRAEL

8. PERFORMING ORGANIZATION REPORT NUMBER

9. SPONSORING / MONITORING AGENCY NAME(S) AND ADDRESS(ES)
U.S. Army Medical Research and Materiel Command
Fort Detrick, Maryland 21702-5012

10. SPONSOR/MONITOR'S ACRONYM(S)

11. SPONSOR/MONITOR'S REPORT NUMBER(S)

12. DISTRIBUTION / AVAILABILITY STATEMENT
Approved for Public Release; Distribution Unlimited

13. SUPPLEMENTARY NOTES

14. ABSTRACT

This final report covers the period August 2015 - May 2016. We continued to pursue our integrated computational design (University of Washington, Seattle, USA) and the experimental approach of directed evolution (Weizmann Institute, Rehovot, Israel), the two basic technologies described and implemented throughout this effort. The achievements during this period, including the isolation of adequately proficient VX and RVX degrading enzyme variants, are summarized on pages 2-3 of this report.

15. SUBJECT TERMS
a. Cloning; expression; X-ray structure; 3D structure; chemical synthesis; GF surrogate, Computational Chemistry

16. SECURITY CLASSIFICATION OF:			17. LIMITATION OF ABSTRACT	18. NUMBER OF PAGES	19a. NAME OF RESPONSIBLE PERSOI
a. REPORT	b. ABSTRACT	c. THIS PAGE			USAMRMC
U	U	U	UU	22	19b. TELEPHONE NUMBER *(include area code)*

TABLE OF CONTENTS

1. Abstract

During the period August 2015 - May 2016 covered by this report we continued to use integrated computational design (University of Washington, Seattle, USA), and the experimental approach of directed evolution (Weizmann Institute, Rehovot, Israel), the two basic technologies described and implemented in our previous Annual Reports, and in doing so met our development targets in full. The following outlines our principal achievements during this period.

1. A multidisciplinary approach combining computational design, directed evolution, and site-directed mutagenesis, based on inspection of docked OP models, was used to enhance the catalytic activity of PTEs towards the toxic enantiomer of Russian VX (RVX). Variant MBP-C23-IVA1-m2p0 hydrolyzed the more and the less toxic RVX enantiomers with k_{cat}/K_M values of $1.15x10^7$ and $4.4x10^6$ $M^{-1}min^{-1}$, respectively. Thus, C23 variants 4E11 and IVA1-m2p0 are the best scavengers of VX and RVX we have had at the last month of funding, at which stage their over-expression and purification commenced. These variants were thus over-expressed, purified and sent to ECBC for further evaluation during May 2016 (>100 mg per variant).
2. Based on previously generated libraries, and on the computationally docked transition state of VX, we generated a gene library using variant C23-m2p0-Y309W as the scaffold gene. Following screening, several clones exhibited up to 2.6-fold improvement in activity on VX relative to the scaffold gene and 4E11. We designed a new library based on C23-m2p0-Y309W that includes both the newly selected random mutations and the mutations appearing in 4E11. This library has been screened and the active variants identified await validation and characterization.
3. In a further attempt to generate and identify new PTE variants with improved VX hydrolyzing efficiencies, we screened a small library of computationally designed variants suggested by the Baker group. Although we used a stabilized starting clone, it is possible that its structure was unable to tolerate the relatively large number of designed mutations, most of which completely changed the physical and chemical nature of the original residues.
4. In continuation of our attempts to develop an HTP screen for OP-hydrolyzing enzymes, we showed that, unlike PTE, PON1 is capable of overcoming the unfolding-refolding barrier *en route* to secretion. Our data indicate the feasibility of secreting a functional OP-hydrolyzing enzyme to the periplasmic space and cell surface of E. *coli*, thus permitting HTP screening of PON1 libraries for variants capable of hydrolyzing various types of nerve agents.
5. To obtain tagless variants, we attempted to express the stabilized variants without the MBP tag. However, the yield of soluble, functional proteins was low. To improve large-scale expression of the tagless forms in various expression systems, we tested vectors that included pET41a (His-GST), pET32b (Trx-His) and pK171 (His-SUMO). We consequently achieved successful isolation of tagless C23-m2p0 using GST-m2p0 and SUMO-C23 as starting points, followed by proteolytic cleavage of the tag and purification of the tagless enzyme.

6. The N-terminus of subunit B of PTE-A53 was shown by X-ray crystallography to protrude into the active site of subunit A in a symmetry-related molecule. In an attempt to obtain information on the mode of binding of V-type nerve agents to PTE, we superimposed a computational model of PTE with the transition state of a V-type nerve agent on the crystal structure of the complex of A53 with methyl phosphonate. This superimposition shows that the predicted binding mode in the computational model is similar to that in the crystal structure of the complex, thus validating our computational protocols and models.
7. Crystals of the over–expressed tagless C23-m2p0 obtained by the ISPC diffracted to 2.3 Å at the WIS X-ray crystallography unit.
8. The tagless C23-A203L variant was over-expressed and purified, and was tested for protection against VX intoxication by Prof. Franz Worek at the Bundeswehr Institute of Pharmacology & Toxicology in Munich (non-funded collaboration). The study demonstrated for the first time the suitability of intraosseous (i.o.) injection of a PTE into VX-poisoned guinea pigs. Intraosseous vascular access systems may allow safe and rapid administration of a catalytic bioscavenger to the systemic circulation, and thus improve the post-exposure PTE therapy of nerve agent poisoning.
9. By computing the energetic effects of residue changes on the PTE structure, as well as the evolutionary scores for residues in the 2nd and 3rd shells, we computationally designed a small library of mutant PTEs anticipated to display increased catalytic efficiency towards RVX and Chinese VX (CVX). To expand the ability of our designed PTEs to neutralize G-type nerve agents, the two most toxic G-agents, soman (GD) and cyclosarin (GF), were also docked into the active site of PTE-C23 and PTE-A53 with their large O-alkyl moieties located in the same pocket of the enzyme that accommodated RVX and CVX. Further computational input was utilized to stabilize the leaving fluoride ion, so as to increase the catalytic activity towards GD and GF. Our computational analysis was in agreement with mutational and kinetic observations made in earlier rounds of experiments on PTE variants. We used the aligned transition-state models to design small libraries of PTE variants, in order to increase catalytic activity towards both RVX and CVX, as well as towards GD and GF. Testing of the second generation of PTE mutants was in process at the time that this funding period terminated. Nonetheless, the preliminary results indicate that the best variants obtained thus far approach the level of catalytic necessary for prophylactic protection against both G- and V-type nerve agents by low protein doses.
10. Finally, we wish to report that during the course of compilation of the Final Annual Report, after the contract had formally terminated, on May 31, 2016, we continued to evaluate several newly designed variants. We found that the best variants displayed k_{cat}/K_M values towards the toxic enantiomer of VX exceeding $5x10^7$ $M^{-1}min^{-1}$ and $9x10^7$ $M^{-1}min^{-1}$ at 25°C and 37°C, respectively. A full account of this achievement, which was set as the principal goal of the project, is being prepared for publication.

2. Introduction

Prophylaxis and treatment during the acute phase of chemical warfare nerve agent (CWNA) poisoning is based on drugs selected to counteract the symptoms caused by accumulation of acetylcholine. Current antidotal regimens consist of pretreatment with pyridostigmine, and of post-exposure therapy that involves administration of a cocktail containing atropine, an oxime reactivator and an anticonvulsant, such as diazepam. The multi-drug approach against CWNA intoxication has been adopted by many countries, and has been integrated into their civilian and military medical doctrines. However, it is well recognized that these drug regimens suffer from several disadvantages that call for new therapeutic strategies. One such approach is to rapidly detoxify the CWNA in the blood before it is able to reach its physiological targets, and one way of achieving this objective is the use of a bioscavenger. The first bioscavengers considered were the stoichiometric bioscavengers, AChE and BChE. However, use of the best stoichiometric bioscavenger currently available (human butyrylcholinesterase, hBChE) requires administration of hundreds of milligrams of protein to confer protection against multiple toxic doses of CWNA (Ashani & Pistinner 2004). *In vivo* protection experiments confirmed the capacity of catalytic scavengers, such as wt OpdA from *Agrobacterium radiobacter* (Bird et al., 2008; Gersham et al, 2010; Jackson et al, 2014), to prevent lethality caused by commercial OP pesticides using as low as 1 mg/kg protein. Thus, attention was turned to the development of catalytic bioscavengers that may be capable of rapidly counteracting nerve agents *in vivo*. The present effort is a continuation of a previous DTRA contract (HDTRA1-07-C-0024), which had as its primary objective the engineering and enhanced evolution of highly proficient universal mammalian recombinant paraoxonases (rePON1s) capable of detoxifying a broad spectrum of G- and V-type nerve agents. The expertise and knowledge gained over the course of the contract, which was accompanied by the evolution of very promising variants capable of rapid detoxification of the nerve agents (both *in vitro* and *in vivo*) strongly supported investment in advanced development of this approach. At the end of the basic base period of the current contract, the SOW was slightly modified so as to focus our ongoing efforts on the generation of V-type hydrolyzing PTE variants, and on improving the biopharmaceutical characteristics and proficiencies of the G-type hydrolyzing variants (for details see below).

The objective of the current effort is to develop a new generation of antidotes against CWNAs, capable of effective catalytic degradation of both G- and V-type nerve agents. We envisage that such employment of the catalytic bioscavenger concept will provide protection against a wide spectrum of CWNAs at protein doses several-fold lower than the hundreds of milligrams doses of human BChE. Recombinant mammalian paraoxonase PON1 (rePON1), and bacterial organophosphate hydrolase (phosphotriesterase; PTE), were selected as possible candidates. These enzymes have the capacity to neutralize CWNAs, but their catalytic efficiency must be greatly improved in order to permit a meaningful *in vivo* detoxification of all types of nerve agents at a low protein dose. We planned to deliver one or more enzyme variants sufficiently potent, and pharmaceutically suitable, to provide protection (either pre- or post-exposure) against G- and V-type nerve agents at protein doses corresponding to ≤50 mg per 70 kg body weight. To achieve this goal, our initial success criterion with

respect to design, generation, and screening for catalytic efficiency of the evolved enzymes was set at $k_{cat}/K_M \geq 1x10^7$ $M^{-1}min^{-1}$, preferably at $5x10^7$ $M^{-1}min^{-1}$. Progress made during the period covered by this report suggests that the latter value is indeed attainable. The greater the k_{cat}/K_M value, the lower the protein dose required (Ashani *et al*, 2016). We also proposed to embark on the improvement of the biopharmaceutical characteristics of promising variants with high catalytic proficiency. Thus, our initial goal was to extend the mean residence time of promising enzyme candidates such that a single shot of <50 mg protein/70 kg will provide adequate protection against a 2xLD50 dose of nerve agent over several days. The use of recombinant proteins as pharmaceuticals poses difficulties with respect to storage stability, bioavailability *in-vivo* and immunoreactivity. It is envisaged that the proposed bioscavengers will be devoid of untoward physiological side effects, and will display long-term storage capacity and extended *in vivo* longevity that will enable them to counteract both acute and long-term exposure to CWNAs.

The benefits of the proposed approach are such that the war fighter will be protected using a low dose of two or more enzyme variants against a broad spectrum of lethal nerve agents at levels exceeding $2xLD_{50}$. Since it is anticipated that prophylaxis with these enzyme drugs will detoxify the nerve agents in the blood, and thus prevent inhibition of physiologically important AChE within target organs, it is envisaged that they will provide 'stand-alone' protection that will obviate the requirement for immediate post-exposure therapy with the standard drug regimen referred to above (*viz.,* the atropine/oxime/diazepam cocktail). Post-exposure treatment in the case of slowly penetrating nerve agents, or of low-level long-term exposure, may be successfully achieved either alone or in combination with the existing standard therapies against nerve agent intoxication. We have shown, in collaboration with Prof. Franz Worek (Bundeswehr Institute of Pharmacology and Toxicology, Munich) that this approach is feasible following VX intoxication (Worek et al., 2014).

3. Highlights of Technical Approaches

We proposed to apply a multidisciplinary approach, involving state-of-the art computational design (David Baker, U Washington), directed evolution and bacterial protein expression using *E. coli* (Dan Tawfik, Weizmann) and determination of protein crystal structures (Joel Sussman, Weizmann). We based our current efforts on our previous accomplishments (contract HDTRA1-07-C-0024). The procedure for repurposing natural metalloenzymes to hydrolyze OPs was previously described and validated using diethylcoumarin phosphate (DECP) as the target molecule (Khare *et al*, 2012). We used the Baker group's computational procedure to design variants specifically tailored for hydrolysis of VX, RVX and CVX (the *O-n*-butyl analog of RVX). Screening of libraries was based on specific medium-throughput screens of active clones by directly assaying for the protection of AChE against all types of nerve agent (Devi-Gupta et al., 2011; Goldsmith et al., 2012; Cherny et al., 2013). V-type nerve agents were obtained in dilute aqueous solution by reacting the corresponding non-toxic components, *O*-alkyl methylphosphonothiolate and the required *N,N*-

dialkylaminoethylchloride. Resolution of the two enantiomers of VX and RVX not only validated protocols in which racemic VX had been employed, but also permitted direct determination of the rates of degradation by PTE of the more toxic and less toxic enantiomers. G-type nerve agents were generated *in situ* by employing a non-hazardous protocol that converted G-agent surrogates to the corresponding nerve agents in dilute aqueous solutions.

Tagging of PTE variants at the N-terminus allowed us to obtain pure preparations that produced crystals diffracting to 1.65-1.7 Å resolution, thus permitting visualization of their entire 3D crystal structures at atomic resolution. The non-active, non-toxic oxo analogs of V-type nerve agents were synthesized, and were employed in attempts to map the active sites of two PTEs designed to interact with either VX or RVX. Several new VX surrogates were synthesized on a milligram scale and used to generate the agents themselves *in situ*. They were employed in the HTP protocol developed for screening large PTE libraries.

To address the need for improved stability and high yield of bacterial over-expression of PTEs we used a fully automated algorithm developed by Sarel Fleishman (Biomolecular Sciences Dept, WIS) to design stable proteins based on atomistic Rosetta modeling and phylogenetic sequence information. This generic method minimizes false-positive predictions to ensure that only a small set of variants (ideally just one) needs to be experimentally tested to achieve high functional yields. This algorithm predicts novel variants displaying enhanced bacterial expression yields and stability, without sacrificing or altering activity (Goldenzweig et al (2016) Automated computational design of human enzymes for high bacterial expression and stability. Mol Cell (in press).

The multidisciplinary capabilities that we have developed, using cutting-edge technologies that include organic synthesis, genetic engineering, computational design and determination of protein crystal structures, will permit further evolution of bacterial PTE and other enzyme templates, to yield bioscavengers with enhanced catalytic and biopharmaceutical characteristics.

4. Detailed Description of Major Achievements

During Option Period 4 (*viz.*, the 5th year of the project), from 07 August 2015 through 31 May 2016 the major tasks performed are described below. The final objective was to deliver the best OPH variants for detoxification of V- and G-agents for further evaluation at ECBC.

4.1 Design and screening of PTE variants hydrolyzing V-type nerve agents

4.1.1 Libraries based on the stabilized m2p0 scaffold

We continued our attempts to improve the catalytic efficiency (k_{cat}/K_M) of PTE variants towards the toxic isomer of VX by employing whole-gene site-directed mutagenesis on the lead variant C23_Y309W. In our previous annual report, covering

08.2014-08.2015, we described the activity and stability of C23_Y309W-derived variants designed to increase thermal stability so as to enhance their expression in *E. coli* in a soluble and active form. Two of these multi-modified variants, dubbed m2p0 and m0p95, exhibit greater thermal stability and affinity for Zn^{+2} ions than the parent scaffold, C23-Y309W. Using information about beneficial mutations identified in previous screens, the docked transition state model of VX, and the stabilized m2p0 scaffold, we generated a new gene library. We focused mutagenesis, in particular, on positions 267, 270 and 271. Results are shown in Table 1.

Table 1 shows the mutational composition and catalytic efficiencies of the best variants selected from this new gene library. Variant 4E11 exhibited a small yet significant increase in activity with respect to the toxic isomer of VX. At 37°C there is another ~1.5-fold increase in k_{cat}/K_M for variant 4E11. However, it should be pointed out that for each mutant the stability of the enzyme at 37°C needs to be dissected from the overall catalytic efficiency observed during VX hydrolysis in the presence of DTNB. For 4E11 we have shown that loss of activity at 37°C, due either to thermal inactivation or to the presence of DTNB, is negligible (see our previous Annual Report, 08.2014-08.2015).

Table 1: Rate of hydrolysis of the toxic (-)VX and racemic RVX by the m2p0 variant further modified by mutations at positions 267,270, 271.

Name of Mutant	Amino acid mutations	(-)VX, k_{cat}/K_m ($x10^6$ $M^{-1}min^{-1}$) at 25°C	(-)VX, k_{cat}/K_m ($x10^6$ $M^{-1}min^{-1}$) at 37°C	Racemic RVX, k_{cat}/K_m ($x10^6$ M^{-1} min^{-1})	
				fast	slow
3B11/2A7*	S267R/A270S/L271W	13.9 ± 2.0	21.2 ± 2.6	1.27±0.30	0.54±0.15
6C12	S267R/A270D/L271W	14.3 ± 1.5	26.0 ± 2.1	1.07±0.02	0.43±0.05
4E11	**S267M/A270S/L271W**	**30.6 ± 3.3**	**41.6± 6.6**	**2.22±0.15**	**0.41±0.03**
6A11	S267R/A270E/L271W	8.6 ± 0.3	N.D	N.D	N.D
6B10	S267R/A270D/L271F	8.8 ± 0.4	N.D	N.D	N.D
1C2	S267R/A270E/L271P	5.7 ± 0.1	N.D	N.D	N.D
C23_Y309W_m2p0 (parent template)	**S267/A270/L271**	**19.5 ± 0.8**	**33.8 ± 4.3**		

*- screening of 96-well plates yielded two variants (3B11 and 2A7) displaying the same sequence

It is worth noting that 4E11, 6C12 and 3B11 display k_{cat}/K_M values of 1-2x10^6 $M^{-1}min^{-1}$ towards the fast isomer of RVX.

The relative activity at 50°C and metal-chelating capacity of 3B11, 6C12 and 4E11 are shown in Table 2.

Table 2: Effects of 50 µM 1,10-phenanthroline and temperature on relative activity of the best variants of C23_Y309W_m2p0 (see Table 1).

Variant	Mutations	Relative V_{max} at 50°C (1)	Relative V_{max} in presence of 50 µM 1,10-phenanthroline (2)
3B11	S267R/A270S/L271W	75.3± 1.9	98.5±2.4
6C12	S267R/A270D/L271W	77.0± 4.3	37.5±1.3
4E11	**S267M/A270S/L271W**	**78.0± 1.4**	**79.2±11.0**

(1) Incubated 30 min and cooled over 10 min to RT. The V_{max} obtained at RT was taken as 100%, and that at 50°C was expressed relative to the values obtained at RT.

(2) The V_{max} obtained in the absence of 1,10-phenanthroline was taken as 100%, and that at 50 µM 1,10-phenanthroline was expressed relative to the values obtained in absence of 1,10-phenanthroline.

Activity was determined using 1 mM paraoxon. The purified MBP-tagged proteins were used to determine thermal stability and metal-chelating capacity.

Encouraged by the above results, we decided to generate gene libraries based on the improved variant 6C12, in an attempt to further increase catalytic activity towards VX. In these libraries we focused on new positions in the active site (*i.e.*, 303, 306, 309 and 310), which were previously not amenable to substitution. The results presented in Table 3 show data concerning introduction of mutations at positions 303, 306, 309, and 310 into the 6C12 variant.

Table 3: Rate of hydrolysis of the toxic enantiomer (-)VX by mutants based on 6C12 (C23_Y309W_m2p0_S267R/A270D/L271W) with mutations at 303, 306, 309, and 310

Variant	Mutations	k_{cat}/K_m x10^6 $M^{-1}min^{-1}$
F12/H12	L303V/F306I/W309Y/V310T	**0.13±0.01**
E12	L303V/F306H/W309Y/V310T	<0.005
C12	L303V/F306H/W309Y/V310A	<0.005
B12	L303T/F306I/W309Y/V310A	**0.017±0.02**
G12	L303V/F306I/W309Y/V310L	0.051±0.01
6C12 , lead variant, C23_Y309W_m2p0_S267R/A270D/L271W	**L303/F306/W309/V310**	**14.3 ± 1.5**

*- screening of 96-well plates gave two mutants, F12 and H12 with same sequence

The 6C12 variant turned out to be very sensitive to changes in the residues belonging to the 'wall' constituted by residues L303, F306, W309, and V310, which appears to simultaneously form close contacts with both the ethoxy methylphosphonyl head and

the *N,N* diisopropyl moiety at the extremity of the leaving group (see Fig. 1). Thus, any of the listed changes produced a decrease in activity towards the toxic isomer of VX of two orders of magnitude or more.

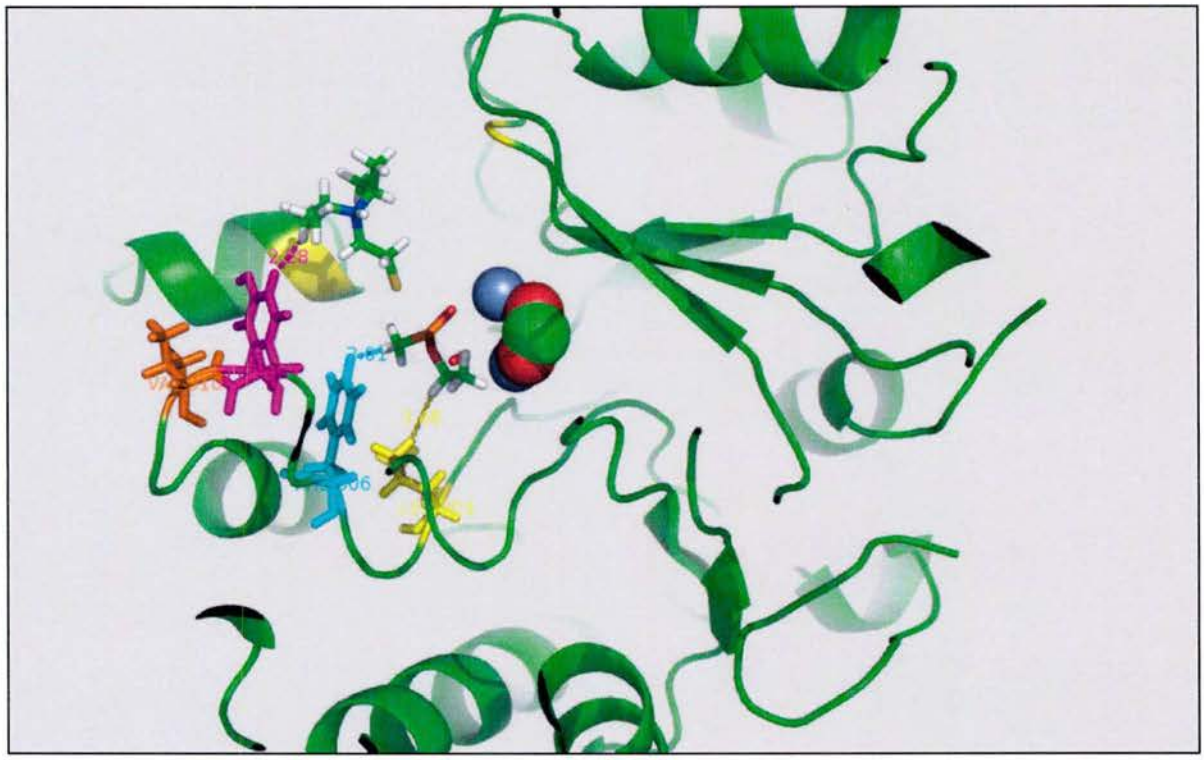

Figure 1: A model representation highlighting the active-site 'wall' composed of residues L303 (yellow), F306 (cyan), Y309 (magenta) and V310 (orange) within the C23 crystal structure. The grey spheres are the two Zn^{2+} ions and adjacent water molecules that are likely to participate in the catalysis. The methyl ethoxyphosphonyl moiety, in contact with residues 303 and 306, detaches from the *N,N*-diisopropylaminoethane thiol, which is in contact with residue 309. This is assumed to result from cleavage of the conjectured transition state for the toxic, S_P isomer of VX.

Similar attempts to mutate 4E11 (C23_Y309W_m2p0_ S267M/A270S/L271W) and 3B11 (C23_Y309W_m2p0_ S267R/A270S/L271W), did not yield any improvement based on assays of variant-expressing bacterial cell lysates. With no improvement in the above libraries, we decided to generate libraries based on random mutagenesis with an average of 1-4 mutations/clone. We decided to generate a random mutagenesis library based on C23-m2p0-Y309W as scaffold. For details of the methodology see the 2nd quarterly report for the current year (07-Nov 2015 to 06-Feb-2016). One variant (3-5A) was repeatedly better than all the others, but was only 1.6-fold better than the control. We sequenced the best 6 clones from the 14 isolated after the first round of screening. Only clone 3-5A had incorporated a mutation, V80M. The rest were identified as C23-m2p0-Y309 (*i.e.*, had not incorporated any random non-silent mutation). When we compared the amino acids that could be found at position 80 in the PTE family alignment (Fig. 2) we found that the substitution to Met had not been observed in any natural PTE family homolog that had been sequenced. Thus, it may be unique to the selection for VX-hydrolysis. However, there is not much

conservation at that position except for the hydrophobic nature of the residue: A, L, F, V, I, Y. We concluded that in constructing future libraries, we should incorporate additional residues at that position to test for improvements in catalytic efficiency towards VX.

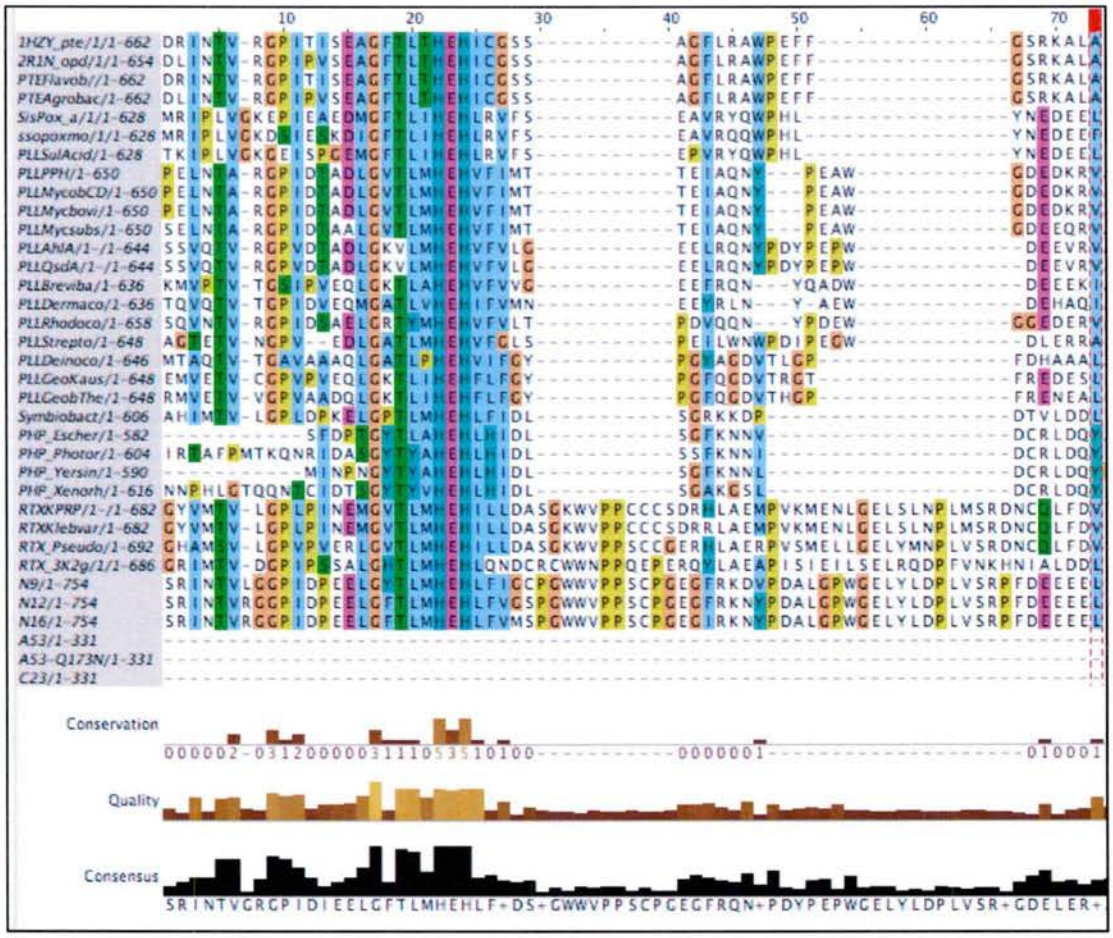

Figure 2: Sequence alignment of PTE family members. Only part of the alignment, taken from Afriat-Jurnou et. al. (2012), is displayed (The alignment starts at position +6, so position 74 is actually 80). The right-most column depicts the residues at position 80 in different PTE family members.

In conclusion, the mutational load of the random library seemed to be optimal for exploring single point mutations. While the identified improvement was modest at the present stage of optimization, the diminishing returns are expected to be high, and a 1.5-fold improvement is meaningful and well worth exploring.

A more exhaustive screen of this library (screening of 12 more plates, ~1050 new clones) resulted in 34 improved clones for verification. Eight clones were selected for sequencing, after exhibiting 1.6-2.6 fold improvement over C23-m2p0-Y309W towards VX in the verification assay. Of the 8 clones sequenced, 3 had incorporated the mutation V80M, 3 had the D233N mutation, an active-site mutation previously selected in rounds 4, 6, and 7 of the PTE evolution, and 1 variant was w.t. (as expected from its

activity). We designed a new library, based on C23-m2p0-Y309W, which includes both the newly selected random mutations and those of 4E11. This library is pending screening for improved VX-hydrolyzing clones.

4.1.2 Computationally designed library

In a further attempt to generate and identify new PTE variants with improved catalytic activity towards VX we decided to screen a small library of computationally designed variants (see below the paragraph on Computational Design presenting results provided by the Baker Group). This library combined functional PTE mutations selected during previous screening rounds and mutations previously reported in the literature to increase PTE's OP-hydrolyzing activity (referred to as GS and TS for ground- and transition-states, respectively). Both kinds of mutations were incorporated on a stabilized PTE variant C23-m2p0-Y309W template. The rationale behind the construction of this library was that a stabilized variant would be able to incorporate additional new mutations without suffering a severe reduction in its stability. Also, that functional PTE mutations previously identified can be combined in new sequence contexts to provide increased catalytic activity on OP substrates. Such functional mutations would be much less likely to destabilize the protein, since they had been previously incorporated into functional PTE variants. Thus, new combinations of mutations, displaying beneficial effects on catalytic efficiency, could be generated, and new improved variants identified in the screen. To this end a library of 43 computationally designed clones was synthesized (Gene9®) and cloned into an expression vector (pMAL-c2, NEB®) using EcoRI and PstI restriction sites. The experimental details of this procedure were described in our 2nd quarterly report for the current year (07-November 2015 to 06-February-2016). Screening was based on measuring residual AChE activity spiked into the protein-expressed library clones, by comparison to a non-AChE-inhibited sample, and was compared to that of similar lysate samples of the template variant C23-m2p0-Y309W, to identify variants with increased VX-hydrolyzing activity. Such variants should display greater residual AChE activity relative to the template variant.

In principle, the size of the designed library (43 clones) is small enough to cover by screening one 96-well plate (*i.e.*, each clone is likely to be represented at least once). However, to ensure full library coverage we picked 540 clones and grew them in 6 deep-well plates. We screened 2 plates using VX and 4 plates using paraoxon. No VX hydrolyzing activity was detected at 150nM and 300nM final VX concentration, in two plates containing 176 random clones (*i.e.*, 4x the library size). In contrast, the template variant, used both for the design and as control in this assay (C23-m2p0-Y309W), was able to hydrolyze 60% and 40% of the VX in the assay (at 150 and 300 nM respectively). The designed clones exhibited on average only 0.13% of the paraoxonase activity of their template variant, C23-m2p0-Y309W (Fig. 3). The maximal paraoxonase activity reached only 1.1% of that of the control template variant.

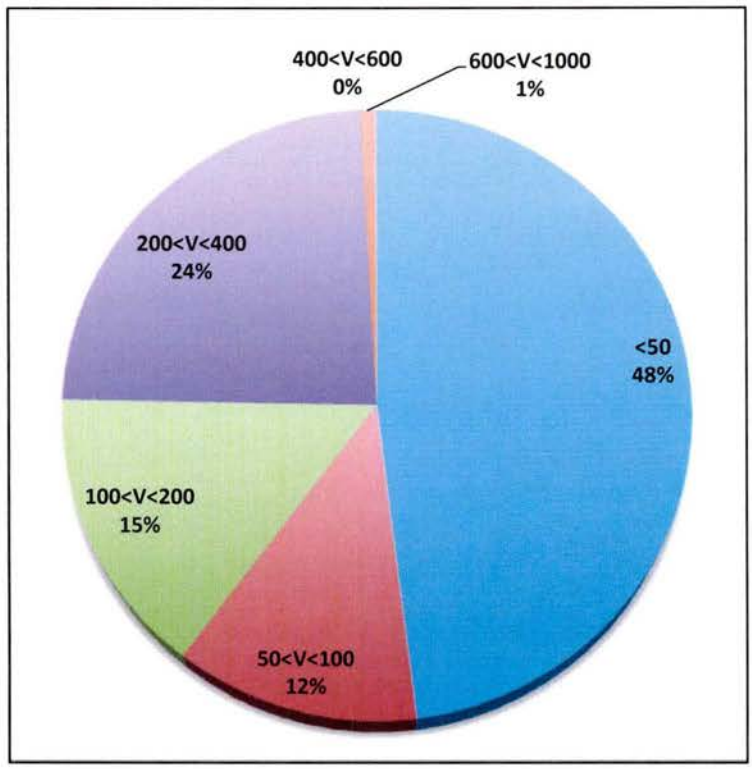

Figure 3. Paraoxonase activity of designed library clones. Distribution of paraoxonase activity of designed PTE clones is displayed in ranges of initial velocities V_0[mOD/min] from low (<50 [mOD/min]) to high (600<V<1000 [mOD/min]) for 360 clones. For comparison, the activity of the template clone C23-m2p0-Y309W was ~75,000 [mOD/min].

We sequenced 4 clones from the library that were screened to make sure that the cloning process was correct. We chose two clones that gave relatively high paraoxonase activity, one with low activity and one with no activity. The clone with paraoxonase-hydrolyzing activity was chosen to identify the inclusion of any deleterious mutation or the existence of insertions and deletions.

We observed the following:

1) All the mutations detected could be traced back to either the GS or TS designs.
2) No insertions or deletions resulting from cloning artifacts were found.
3) There seemed to be a good correlation between sequence and function:

The clone with very low activity suffered a E132T mutation. This is a critical position in PTE, and Thr at this position (unlike Glu) is not a mutation that we have observed in any PTE family members. The clone that was devoid of activity could not be sequenced. This usually indicates that the gene had not been inserted, and that the plasmid is an empty vector contamination, which is not a unusual phenomenon. The two clones active towards paraoxon had 6-7 mutations per gene, which could explain their low overall activity relative to the starting point clone. Still, they had a lower mutational load than the average in the library (10.5 per gene), which may explain why

they are better than the average in the library. In the following we detail the analysis of the above mentioned results:

a) In the designed clones provided by the Baker Group both Ground-State (GS) and Transition-State (TS) groups contained on average 10.6 ± 6 mutations per variant (relative to the starting point), at 36 positions throughout the gene (**Table 4**).

b) The minimal number of mutations per clone was 4, the maximum 23.

c) In the GS group, we found on average 9±5 mutations that changed the character of the original amino acid (*e.g.*, polar to aliphatic, negative to polar, polar to hydrophobic, etc.). The TS group was not similarly analyzed, but is likely to follow the same pattern.

Table 4: Analysis of unselected clones from the designed library

	GS clones	TS clones
Number of clones	25	18
Mutations per gene	10.6 ± 6	10.3 ± 5.5
Max mutations	21	23
Min mutations	4	5
# of positions mutated	36	35

To summarize:

1) It seems that the new designs may be overloaded with mutations. Whereas some mutations may be beneficial, others may result in reduced activity and/or stability (*i.e.*, soluble expression). Although we used a stabilized starting clone, its structure may have not been able to tolerate the relatively large number of mutations introduced, most of which completely changed the physical and chemical nature of the original residues.

2) We have not compared the expression levels of the designed clones and their starting point variant. However, based on past experience we expect to find much lower levels of expression of soluble-active protein in the lysates of the designed clones.

   It is also possible that a redesign of an already shaped active-site, as is the case for C23 and its related variants, is not feasible. Such an attempt has not yet been reported in the literature; thus, the design methodology may need to be redefined to achieve this goal.

4.1.3 Improvement of PTE catalytic activity against Russian VX (RVX)

Variant IV-A1 was earlier reported as the best RVX-hydrolyzing PTE that we had yet obtained (Goldsmith et al, 2015). To further enhance its activity, the mutations of this variant (Table 5), were cloned individually and simultaneously into C23-m2p0-Y309W.

Table 5: Comparison of the mutations of C23 and IV-A1

Selection round	7	0	5
Amino Acid	IV-A1	PTE-wt-S5	C23
59	M	C	C
77	A	K	A
80	V	A	V
106	A	I	I
132	E	F	E
173	N	T	N
203	A	A	A
204	A	A	A
208	D	G	D
233	G	D	D
254	G	H	G
266		A	A
270	A	A	A
274	N	I	N
319	S	S	S
342	S	P	S

The library was screened with RVX, and the combined-mutations clone defined as MBP-IVA1-m2p0-Y309W was found to be the most active variant towards the toxic isomer of RVX. Thus, in addition to the added segment of the stabilizing core of m2p0, the IV-A1 variant was also mutated at position 309 to replace Tyr with Trp. Its catalytic activity is summarized in Table 6.

Table 6: Catalytic activity of variant MBP-IVA1-m2p0-Y309W determined for V-type agents employing the DTNB protocol (Tris, 50 mM NaCl/50 mM Tris, pH 8.0, 25°C)

Catalytic Activity , k_{cat}/K_M (±SD; n=2-3) x 10^6[$M^{-1}min^{-1}$]					
VX[a]		RVX[a]		CVX[b]	
Sp	*Rp*	*Sp*	*Rp*	fast	slow
3.46 ±0.2	0.48 ±0.06	11.55 ±1.3	4.45 ±0.6	6.12 ±0.95	1.2 ±0.1

a. The VX and RVX enantiomers were prepared on a milligram scale in our laboratory according to Berman & Leonard (1989). Optical purity was >95%. Data points were fitted to a mono-exponential association function.

b. The racemic Chinese VX was synthesized on milligram scale in our laboratory. Data points were fitted to a bi-exponential association function keeping the two phase amplitudes at 50% each.

Results shown in Table 6 clearly highlight the importance of the active site architecture of PTE in its action on various V-type agents bearing different alkyl moieties attached either to the P atom or the N-containing side chain of the leaving group. It should be pointed out that the less toxic enantiomer of RVX (the *R*p isomer) is hydrolyzed rapidly by MBP-IVA1-m2p0-Y309W. In fact, the combination of 4E11 and MBP-IVA1-m2p0-Y309W covers the required catalytic activity for reasonable *in vivo* detoxification of both stereo-isomers of V-type nerve agents. In addition to its high catalytic activity towards the toxic isomer of RVX, MBP-IVA1-m2p0-Y309W catalyzes the hydrolysis of the two toxic diastereoisomers of soman (GD) at similar rates. During the evolution of the PTE-C23 scaffold we observed an early decrease of stereoselectivity towards the 2 toxic isomers of GD (*Sp*Rc and *Sp*Sc) wherein the time course of loss of of anti-AChE activity changed from a bi- to a mono-exponential decay function (Cherny et al, 2013). In the MBP-IVA1-m2p0-Y309W this feature was maintained, and an average detoxification rate constant of 0.97 ±0.19x10^6 $M^{-1}min^{-1}$ was recorded for the complete loss of its anti-AChE activity (using the residual AChE-time course activity protocol) by fitting to mono-exponential decay. Notably, this activity is lower by approximately 8-fold than that of the lead variant C23 on GD (Cherny et al, 2013). It will be worth completing a full study of the catalytic activity of MBP-IVA1-m2p0-Y309W and of its parent variants C23-Y309W and 4E11, acting on GA, GB, GD, and GF. Our initial data suggest that GF is catalyzed at 2.5x10^6 and 1.5x10^6 $M^{-1}min^{-1}$ by 4E11 and C23-Y309W, respectively (at 25°C).

4.1.4 Temperature coefficient for selected C23 variants

The initial criterion for success in generating PTEs for *in vivo* protection was set at k_{cat}/K_M ≥1x10^7 $M^{-1}min^{-1}$ when reacting with nerve agents. Since the theoretical calculations of the time required to hydrolyze 96% of the OP substrate *in vivo* depends

on the expected k_{cat}/K_M values at 37°C (Ashani et al, 2016), and since our data thus far were obtained on the basis of measurements made at 25°C, we used the two enantiomers of VX and of RVX to determine the temperature coefficients of selected PTEs. Results are summarized in Table 7.

Table 7: Catalytic activity of selected PTEs at 25°C and 37°C.
k_{cat}/K_M (±SD) x10^6 $M^{-1}min^{-1}$ determined by use of the DTNB protocol (50 mM NaCl/50 mM Tris, pH 8.0). The numbers in brackets are SD and figures in red note the ratio of k_{cat}/K_M at 37°C compared to 25°C.

Variant	*Sp*-VX		*Rp*-VX		*Sp*-RVX		*Rp*-RVX	
	25°C	**37°C**	**25°C**	**37°C**	**25°C**	**37°C**	**25°C**	**37°C**
S5[a]	0.015 (0.001)	0.08 (0.04)	0.034 (0006)	0.055 (0.001)	0.002	0.009	0.055 (0.007)	0.09 (0.05)
C23	7.9 (0.75)	15.4 (0.6)1.9	0.60 (0.01)	1.8 (0.2) 3.0	0.67 (.10)	2.2 (0.5)3.3	3.1 (0.35)	8.1(1.1) 2.6
A203L	9.2 (0.95)	20.1 (1.5)2.2	0.67 (0.035)	1.9(0.2) 2.8	0.74 (0.06)	2.5 (0.4)3.4	2.8 (0.03)	7.5 (0.9) 2.7
Y309W	14.7 (1.0)	28.9 (0.7)2.0	0.82 (0.07)	2.2(0.2) 2.7	1.42 (0.18)	4.2 (0.3)2.9	4.5 (0.75)	20.2(5.2) 4.5
4E11[b]	19.0 (2.2)	36.1 (1.4) 1.9	0.68 (0.10)	1.5(0.01) 2.2	1.9 (0.55)	4.9 (0.5)2.6	0.53 (0.08)	1.5 (0.5) 2.8
1A12	11.2 (0.95)	21.3 (4.4) 1.9	0.48 (0.06)	1.1(0.03) 2.3	1.13 (0.18)	3.2 (0.6)2.8	0.37	1.0 (0.1) 2.7

a. The 37°C to 25°C ratios for the wt S5 were not calculated, due to the relatively low k_{cat}/K_M that introduces large errors in the estimated ratios. b. Data for this variant were collected with a different batch than that listed in Table 1.

Results show inn Table 7 suggest that for theoretical calculations of the time required to sequester a given amount of the OP in the circulation in the presence of a known concentration of the PTE at 37°C (Ashani et al., 2016) we can safely assume an increase of 2-fold in catalytic efficiency determined *in vitro* at 25°C, and in some cases an even higher increase is observed. Our data also suggest that the less toxic *R*p enantiomers of VX and RVX are likely to be rapidly hydrolyzed by the leading variants under *in vivo* conditions. It should be pointed out that when running the experiments at 37°C one must ascertain that during the time span of data collection the PTE activity does not decrease due to thermal instability.

4.1.5. Generation of a novel system for high-throughput screening of libraries of OP-hydrolyzing enzymes

As described in our earlier reports, we have developed a new paradigm for high throughput (HTP) screening of PTE variants aimed at improving selection of variants

with high activity towards nerve agents from large libraries. The rationale underlying this approach is as follows: It involves attempts to engineer *E. coli* strain that are completely dependent on OP nerve agents as their source of the phosphorus required for their growth. PTE is expected to hydrolyze OP nerve agents to methylphosphonate monoester. Subsequent hydrolysis, catalyzed either by endogenous bacterial enzymes or by introduced phosphonate monoesterase (PMH), should then give rise to methylphosphonic acid, which has been shown to be utilized by *E. coli* as a sole phosphorus source (Fig 4). The growth rate of the engineered bacteria is then expected to parallel the catalytic efficiency of the expressed PTE variant.

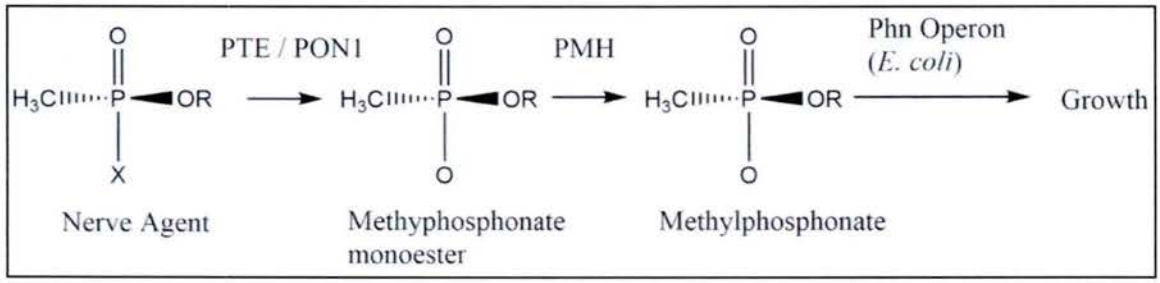

Figure 4: Enzymatic hydrolysis of nerve agents into methylphosphonic acid

Since utilization of methylphosphonate esters is believed to occur within the periplasmic space of *E. coli*, our efforts were focused on secreting PTE to the periplasmic space and to the cell surface of *E. coli*. For this purpose, we genetically fused various signal peptides to the N-terminus of PTE. These signal peptides included TorA, which functions through the twin-arginine periplasmic secretion system, PelB, which recruits the sec pathway for periplasmic secretion, the original periplasmic signal peptide of PTE, and Lpp-OmpA, which is composed of the N-terminal domain of murein lipoprotein from *E. coli*, and of a 113-amino-acid domain from the *E. coli* cell-surface protein, OmpA. The mechanisms of periplasmic/cell-surface secretion involve unfolding of the secreted protein, followed by its refolding in the target cellular compartment. Proteins that are not able to cross the barrier are not expected to form a functional form in the compartment of destination.

In order to monitor periplasmic secretion of PTE, *E. coli* cells were transformed with the respective constructs, grown in LB at 37°C, and induced with 0.2 mM IPTG. Subsequent to centrifugation of the cultures, we determined the paraoxonase activity of the lyzed cell pellet and of the medium (Fig. 5). Due to the relative leakiness of the bacterial cell membrane, we assumed that a significant amount of the secreted proteins that managed to make their way to the periplasmic space or to the cell surface would detach from the cells, and would be found in the medium. Cytoplasmic proteins should be expected to be less abundant in the medium, and more abundant in the cell lysate. Therefore, comparing paraoxonase activity of the medium and of the lyzed pellet for the various constructs can provide an indirect measure of functional secretion. The OP-hydrolyzing enzyme PON1, which has a protein fold different from that of PTE, was also tested for functional secretion into the periplasm and to the cell surface.

Our data show that whereas a PTE construct devoid of a signal peptide is highly active in both the cell pellet and in the medium, PTE fused to a signal peptide displays poor activity in the medium into which it is supposed to be secreted (Fig. 5), indicating poor secretion of functional PTE. TorA-PTE is highly active in the lysate, rather than in the medium, indicating that it is not secreted into the periplasmic space. However, TorA-PON1 and Lpp-OmpA-PON1 display higher paraoxonase activity in the medium than PON1 lacking a signal peptide (Fig. 5), indicating significant functional secretion of PON1 to the periplasm and to the cell surface. We conclude that, unlike PTE, PON1 is capable of overcoming the unfolding-refolding barrier *en route* to secretion.

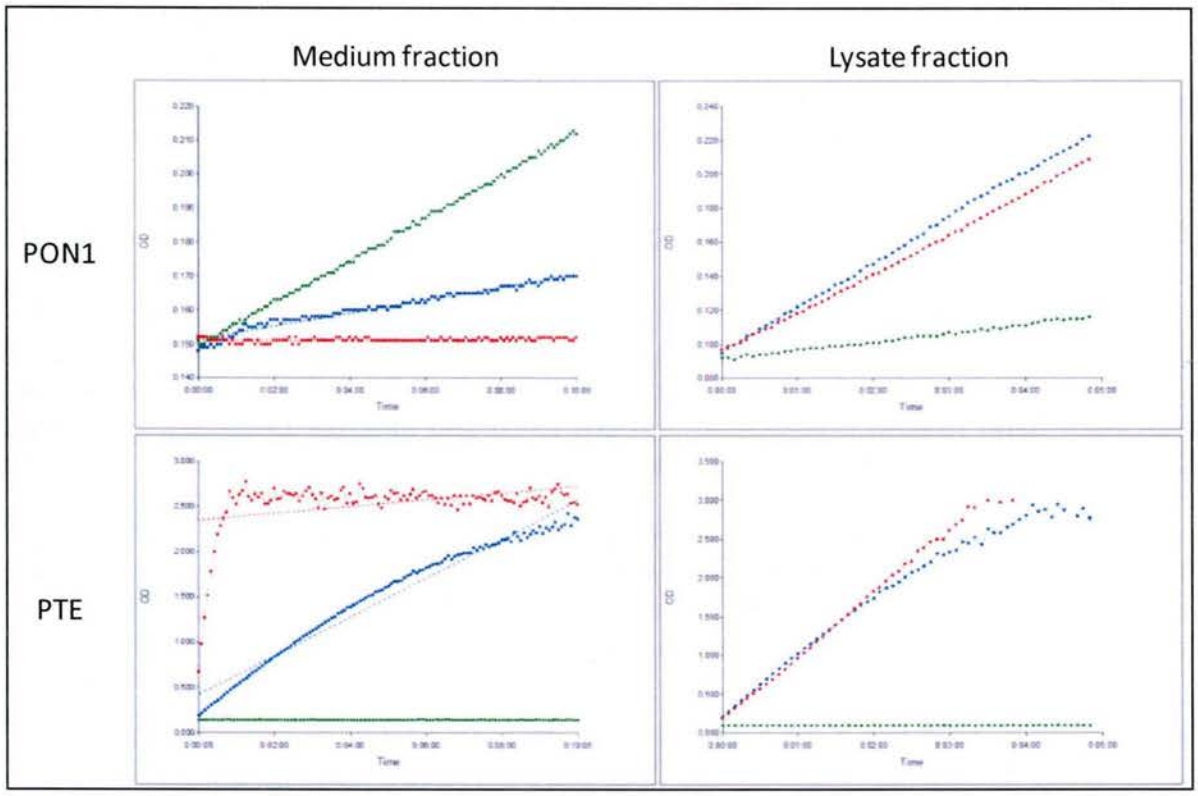

Figure 5: Functional secretion of PON1 and PTE to the periplasmic space and to the cell surface of *E.* coli. Paraoxonase activity of 10 µl of each fraction was assessed for the capacity to hydrolyze 0.4 mM paraoxon. Red curves represent constructs lacking a signal peptide, blue curves represent TorA constructs, and green curves represent Lpp-OmpA constructs. Constructs of PTE and PON1 fused to PelB, and PTE fused to its original periplasmic signal sequence, did not show any activity in either medium of lysate (data not shown).

These results indicate the feasibility of secreting a functional OP-hydrolyzing enzyme to the periplasmic space and cell surface of *E. coli*, thus permitting HTP screening of PON1 libraries for variants capable of hydrolyzing various types of OP nerve agent.

We plan to examine surrogates of nerve agents as the sole phosphorus source for a PON1-expressing evolved strain. The first surrogate to be tested *in vitro* as a substrate for various PON1 variants was *O,O*-diethylpyromethylphosphonate, $CH_3P(O)(OEt)$-O-$P(O)(OEt)CH_3$. Unlike real nerve agents, the leaving group of this surrogate is not toxic

to bacteria, thus permitting clear evaluation of the dependency of growth on the hydrolytic action of PON1.

The advantages of the HTP screen outlined above are:

1. That it will permit faster evolution of efficient OP-hydrolyzing enzymes.
2. That it will permit identification of novel OP-hydrolyzing enzymes from large metagenomic gene libraries.
3. That it will allow rapid adaptation of currently evolved variants to new OP nerve agents.
4. That it will enable bioremediation of surfaces, terrain and equipment contaminated with a broad spectrum of OP-based threat nerve agents.

4.1.6 Improvement of the large-scale production and purification of tagless PTE variants

For achieving the ultimate goals of this project *i.e.*, to carry out animal studies, to obtain high resolution X-ray structure of improved PTE variants, and to modify pharmaceutical properties of scavenger candidates, it is crucial to obtain substantial amounts of improved variants devoid of the maltose-binding protein (MBP) tag. Until now, we had been obtaining tagless improved variants of PTE based on the C23 template using amylose beads, followed by digestion with factor Xa, and finally amylose bead and anion exchange chromatography, to separate PTE from any residual MBP or uncleaved MBP-PTE. However, recently obtained improved variants, namely C23-m2p0-Y309W and 4E11, which contain the m2p0 scaffold, tend to have a pI similar to that of MBP, which makes it difficult to separate MBP and the desired particular PTEs from each other.

To obtain tagless improved variants of PTE, we cloned the C23_Y309W_m2p0, C23_Y309W_mop45, C23_Y309W_mop95 and C23-Y309W, all devoid of MBP, into the pMAL vector. The preliminary expression studies on the tagless proteins shows no overexpression of the above mentioned variants. A good overexpression of tagless stabilized proteins would have paved the way to purifying the tagless proteins in large amounts by conventional protein chromatography methods.

Since tagless stabilized variants failed to express as soluble proteins at high yields, we are attempting to clone the best PTE variants obtained so far, namely C23, C23-Y309W, C23_Y309W_m2p0, C23_Y309W_mop95 and 4E11(C23_m2p0_Y309W_(S267M/A270S/L271W) in various expression systems. The expression vectors employed include pET41a (His-GST), pET32b (Trx-His) and pK171 (His-SUMO). We describe below the successful over-expression of tagless PTE-C23-m2p0 using GST-m2p0, and PTE-C23 using Sump-PTE-C23

PTE-C23-m2p0: *E. coli* BL21 cells were transformed with the GST-C23-m2p0 plasmid. The cultures supplemented with 100µg/ml ampicillin were grown overnight at 37°C. 1% inoculums of these cultures were used to subculture 1.25 L of Luria Broth (LB) supplemented with 100µg/ml ampicillin and 0.2 mM $ZnCl_2$. When the cultures had reached OD = 0.6-0.8, they were induced with 0.4 mM IPTG, followed by growth for 14

h at 20°C. They were then pelleted by centrifugation for 10 min at 7,500 rpm. The pellet was resuspended in 50 ml of buffer A (0.1 mM $ZnCl_2$/0.2 M NaCl/ 20 mM Tris, pH 8.0), supplemented with 1 µl/ml of benzonase, 1µl/ml PIC and 10 µl/ml lysozyme. The cells contained in 50 ml of buffer A were disrupted in a cell disruptor (25000 psi, 4 passes). The cell lysate was centrifuged at 10000 rpm for 30 min. The clarified pooled supernatants from the entire 1.25 L culture were loaded onto 15 ml of a GST bead column (Genescript), which had been pre-equilibrated with buffer A at room temperature. The column was then washed with 15 ml column volumes (CVs) of buffer A. GST-m2p0 was eluted from the GST beads with 4 CV of buffer A containing 10 mM glutathione. The GST-C23-m2p0 was then left at 4°C for 7-10 days, during which period the GST cleaved from the PTE. Subsequent passage through the GST column yielded tagless C23-m2p0, since the GST was retained on the column. The C23-m2p0 was concentrated to ~13 mg/ml in 0.1 mM $ZnCl_2$/0.1 M NaCl/10 mM $NaHCO_3$/0.1 M Tris, pH 8.0, and its purity was checked by 12% SDS-PAGE (Fig. 6).

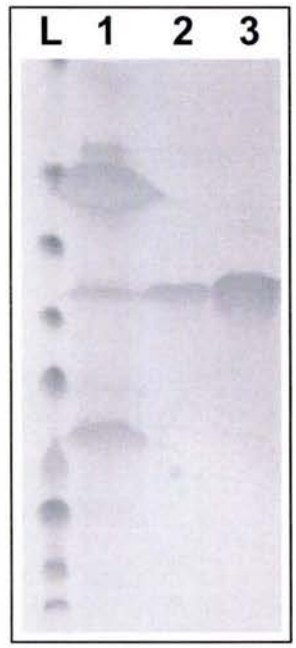

Figure 6: SDS of C23-m2p0 after partial and total cleavage of GST- C23-m2p0. L - protein markers; 1 - after partial autodigestion; lanes 2 and 3 - flow-through from the GST column after complete autodigestion

PTE-C23: Expression of PTE-C23 was performed in the expression vector K151 (His14-bdSumo, Frey & Gorlich, J Chromatog A, 1337 (2014) 95-105).

His-Sumo-PTE constructs were established by using the Transfer-PCR (TPCR) cloning reaction with the following primers:

bdSumo_Ala_PTE_F

GAAATCGACGCAATGCTTCATCAGACTGGTGGCGCGGGAAGGATTTCAGAATTCA TCACCAAC

bdSumo R*-PTE_R

CAACAGGAGTCCAAGCTCAGCTAATTAAGCTTTTATTAAGAAGCACGGAGGGTTG
GAGACAGG

Expression was performed in *E. coli* BL21(DE3) using 200 μM IPTG as inducer, at 15°C for ~18 h. Following cell extraction, the fusion protein (His-Sumo-PTE-C23) was absorbed on A Ni-resin. Following several washing steps, the PTE-C23 was cleaved by a bdSumo protease to obtain a highly purified tagless PTE-C23 at 35-50 mg/L

4.1.7 PK studies in rats

PK studies had two purposes: (a) To establish baseline data in rats to be used as criteria for subsequent modification aimed at increasing the biological half-life of PTEs; (b) to ascertain reasonable residence time in the circulation, and thus confirm that mutations in new and active variants did not significantly reduce availability in blood. Following approval by the DTRA animal committee we initiated and established the PK baseline for a variety of promising PTE candidates. Representative time course profiles in rats following i.v. injections at 1 mg/kg are displayed in Fig. 7.

In view of the rapid clearance of all variants tested the data points were fitted arbitrarily to an apparently mono-exponential decay function. In general, the estimated $t_{½}$ in plasma was 20-35 min. For example, the average $t_{½}$ of the MBP-C23-Y309W variant (Fig. 7A, #1,2,3; $t_{½}$= 26 min) was similar to that of MBP-C23-Y309W-m2p0 (#, 3,4,5, $t_{½}$=24 min). When the MBP tag was removed (Fig. 7B), the $t_{½}$ was moderately increased for C23-Y309W (#, 1,2,3, $t_{½}$=34 min) and decreased for C23-Y309W-m2p0 (# 4,5,6, $t_{½}$=20 min). We also observed differences in the interpolated t=0 plasma concentrations of the injected PTEs. Thus, the presence of m2p0 in the MBP fusion (Fig 7A) gave higher initial plasma levels, whereas in the tagless proteins the m2p0 decreased the initial PTE concentration at t=0 (Fig 7B). These variations may indicate different initial volumes of distribution that depend on either the presence or absence of the tag or the m2p0 insert or a combination of both modifications.

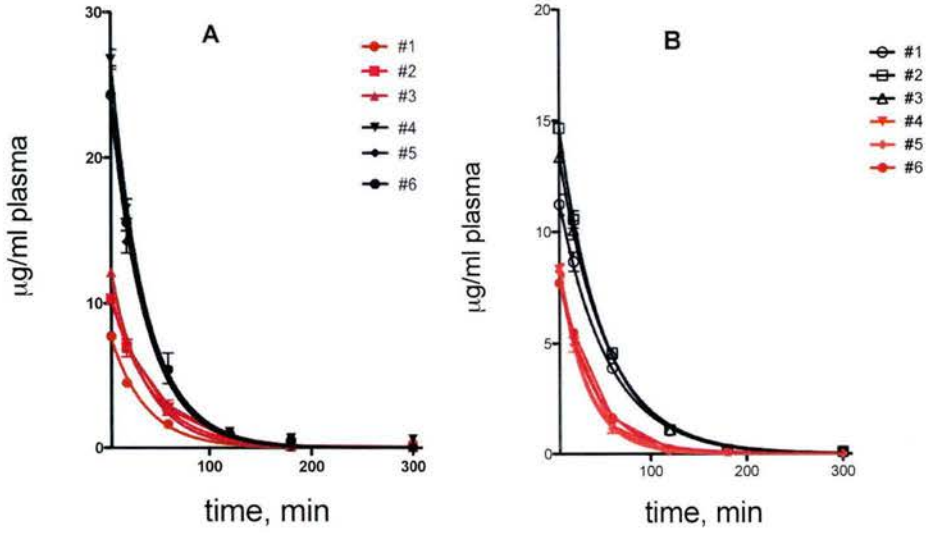

Figure 7: PK in rats injected i.v. with selected variants. A: 1 mg/kg of MBP-C23-Y309W #1, 2, 3) and MBP-C23-Y309_m2p0 (# 4, 5, 6). B: 1 mg/kg tagless C23-Y309W (# 1, 2, 3) tagless C23-Y309W-m2p0 (#4, 5, 6).

We consider the PK studies as exploratory and range-finding experiments. Clearly, more experiments are required, in a range of animal models, to characterize the bioavailability properties, and to attempt to improve biological residence times by chemical modifications or by molecular engineering. Yet, we conclude the following:

a) Tagless PTE behaves like tagged PTE (*i.e.*, now that we do not depend on the immunogenic MBP moiety *in-vivo* because we can cleave it off while still maintaining activity).

b) The stabilized scaffold with the m2p0 insert behaves like the m2p0-free variant (i.*e.*, we did not lose *in-vivo* availability by switching to a stable scaffold).

c) Variant C23-A203L which gives $t_{1/2}$ = 25 min in rats, gives $t_{1/2}$ = 2 h in guinea pigs (Worek et al., 2016). In all likelihood, the rapid rat metabolism affects clearance, and thus call for a battery of animal models to be employed for PK evaluation.

d) The differences in initial plasma levels could be due to experimental errors, and the experiments need to be repeated with different batches of the same protein.

4.1.8 Delivery of 4E11 and IVA1-m2p0 to ECBC

This year we were committed to sending 100 mg of each of our best variants to ECBC. The procedures outlined below describe the over-expression and purification of large quantities of MBP-4E11 and MBP-IVA1-m2p0. These samples were delivered to Dr. S. Harvey at the ECBC on May 30th, 2016):

E. coli GG48 cells were transformed with the MBP-IVA1-m2p0 and MBP-4E11 plasmids. The cultures, supplemented with 100µg/ml ampicillin, were grown overnight at 37°C. 1% inoculums of these cultures were used to subculture 6.25 L of 2YT

supplemented with 100µg/ml ampicillin and 0.2 mM $ZnCl_2$. When the cultures had reached OD = 0.6-0.8 they were induced with 0.4 mM IPTG, followed by growth for 14 h at 20°C. They were then pelleted by centrifugation for 10 min at 7,500 rpm. The pellet was resuspended in 200 ml of buffer A (0.1 mM $ZnCl_2$/0.1 M NaCl/10 mM $NaHCO_3$/100 mM Tris, pH 8.0), supplemented with 1 µl/ml of benzonase, 1µl/ml PIC and 10 µl/ml lysozyme. The cells contained in 50 ml of buffer A were disrupted using a cell disruptor (25000 psi, 4 passes). The cell lysate was centrifuged at 10000 rpm for 30 min. The clarified pooled supernatants from the 1.25 L culture were loaded onto 15 ml of an amylose bead column (NEB BioLabs) that had been pre-equilibrated with buffer A at room temperature. The column was then washed with 15 CVs of buffer A. MBP-IVA1-m2p0 was eluted from the amylose beads with 4 CV of buffer A +10 mM maltose. The eluted MBP-IVA1-m2p0 was dialyzed overnight against buffer A. The dialyzed proteins weres loaded onto an ion exchange column (Tricorn Q10/ 100GL) to get rid of lipopolysaccharides believed to be toxic to the animals used in our studies. The flow through from the ion exchange column, containing either MBP-IVA1-m2p0 or MBP-4E11, was dialyzed against 10 uM $ZnCl_2$ /100 mM NaCl/50 mM Tris, pH 8.0, and its purity was checked by 12% SDS-PAGE (Fig. 8).

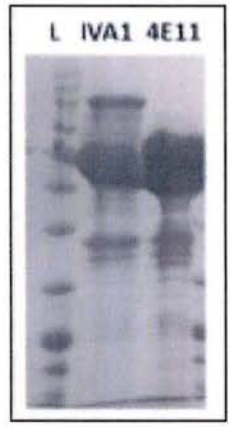

Figure 8: SDS-PAGE on 12% acrylamide gels of purified MBP-IVA1-m2p0 and MBP-4E11 obtained after successive purification on amylose beads and an ion exchange column.

The total amounts of purified proteins obtained were 111 and 141 mg of MBP-IVA1-m2p0 and MBP-4E11, respectively.

4.2 Structural Studies

During the 4th Option Year, the structural studies on phosphotriesterase (PTE) described in the Annual Report for the 3rd Option Year were extended. Some of these studies were concerned with the PTE_C23 and PTE_A53 scaffolds, with the corresponding A203L mutants, *viz.*, PTE_C23_A203L and PTE_A53_A203L, and with their complexes with various relevant phosphonate analogs and fragments that are displayed in Fig. 9. Since these scaffolds were shown to act as highly potent bioscavengers, both *in vitro* and *in vivo*, it was important to clarify the structural features of their active sites that contributed to their efficacy.

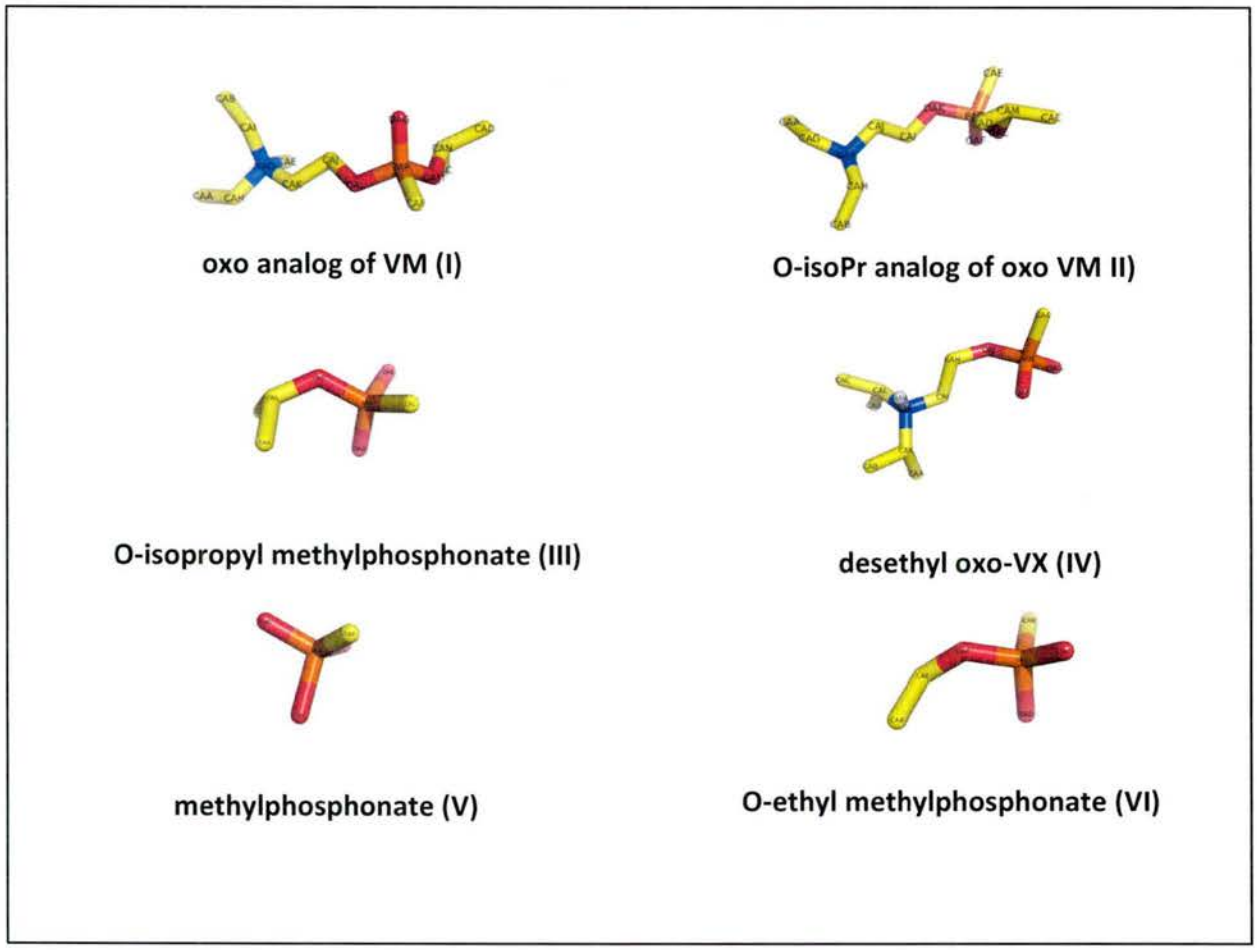

Figure 9: OP compounds co-crystallized with or soaked into crystals of A53 and C23. The oxo analogs of VM and VX are $CH_3P(O)(OEt)OCH_2CH_2N(R)_2$, where R = Et and iPr, respectively. Thus, the structure of IV is $CH_3P(O)(OH)OCH_2CH_2N(iPr)_2$.

In some cases, the PTE variants crystallized were expressed in their native form, and purified by conventional purification techniques. In most cases they were expressed as constructs in which a maltose-binding protein (MBP) tag was fused to their N-terminus, so as to facilitate purification on an amylose-agarose affinity column. The MBP was then cleaved off with Factor Xa, generating PTE bearing a residual ISEFITNS sequence from MBP at its N-terminus. This is not a trivial point, since in certain cases in which the PTE crystallized as a dimer, the octapeptide of one subunit was found to penetrate the active site of the second one, so that only the first was free to complex with the phosphonate analogs and fragments referred to above.

The principal PTE_A53 and PTE_C23 crystal structures described and analyzed in the present report are listed in Tables 8 and 9, respectively. Apo-PTE_A23 and Apo-PTE_C53, purified without the MBP fusion tag, yielded poor crystal structures (#1 in Table 8, and #11 in Table 9, respectively), and were not studied further. All the other samples were purified with the MBP tag, which was then removed with Factor Xa.

Table 8: Summary of PTE A53 data sets

Data set	Protein Sample Dubbed	Crystallization conditions	Resolution Å	Copies in AU	Space Group	Comments
1	PTE_A53 Apo enzyme	10% PEG-6000 5% MPD 0.1M HEPES, pH 7.5	2.0	1	$P22_12_1$	There is only one Zn^{+2}, and electron density seen in the active site cannot be easily interpreted.
7	PTE_A53_Apo 1 Apo enzyme	100mM Tris, pH 7.5 1.5M $(NH_4)_2SO_4$ 17% glycerol	1.77	1	$P4_12_12$	Extra electron density within the active site, but it is not SO_4^{-2}
8	PTE_A53_OXOXO_VX-OH OP **IV** soaked in	100mM Tris, pH 7.0 1.5M $(NH_4)_2SO_4$ 12% glycerol	2.0	1	$P4_32_12$	Electron density seen can be fitted as, **V**
9	PTE_A53_PP OP **V** soaked in	100mM Tris, pH 7.5 1.5M $(NH_4)_2SO_4$ 12% glycerol	1.85	1	$P4_32_12$	Electron density seen can be fitted as **V**
10	PTE_A53_EMP OP **VI** soaked in	0.1M HEPES, pH 7.5 22% polyacrylic acid-5100, sodium salt 0.02M $MgCl_2$	1.75	2	$P2_1$	Electron density corresponds to polyacrylic acid, not to **VI**

Table 9: Summary of PTE C23 data sets

Data set	Protein Sample	Crystallization conditions	Res Å	Copies AU	SG	Comments
11	PTE_C23_Apo Apo enzyme	100 mM HEPES, pH 7.5 15% MPD 10% PEG-6000	2.80	4 (2 dimers)	$P2_12_12_1$	The overall electron density is of poor quality
14	PTE_C23_M Apo enzyme	100 mM HEPES, pH 7.5 26% polyacrylic acid-5100, sodium salt 0.02M $MgCl_2$	1.95	2	$P2_1$	Apo, only Zn^{+2} and 2 waters seen in active site
12	PTE_C23_MO OP **I** soaked in	100mM Tris, pH 7.0 1.5M $(NH_4)_2SO_4$ 17% glycerol	1.77	1	$P4_32_12$	SO_4^{-2} in the active site
13	PTE_C23_MP OP II soaked in	100mM Tris, pH 8.0 1.0M $(NH_4)_2SO_4$ 12% glycerol	1.77	1	$P4_32_12$	SO_4^{-2} in the active site
15	PTE_C23_PP OP **V** soaked in	100mM Tris, pH 8.5 1.5M $(NH_4)_2SO_4$ 17% glycerol	1.85	1	$P4_32_12$	Electron density corresponds to, **V**
16	PTE_C23_OX OP **IV** soaked in	100mM Tris, pH 7.0 1.5M $(NH_4)_2SO_4$ 17% glycerol	2.05	2	$P2_12_12_1$	Electron density corresponds to, **V**
21	PTE_C23_EMP OP **VI** soaked in	100mM Tris, pH 7.5 1.M $(NH_4)_2SO_4$ 12% glycerol	1.80	2	$P4_12_12$	Electron density corresponds to, **V**

Table 8 also displays data for PTE_A53 crystal structures obtained from the MBP-PTE fusion constructs, one apo (#7), and three putative complexes (#8-10), all four diffracting to 2 Å or better. #8 and #9 were soaked in the oxo analog of VX (**IV**), and in methyl phosphonate (**V**), respectively (see formulae in Fig, 9); in both cases electron density corresponding to **V** could be clearly distinguished within the active site. Since there is no reason to expect that **IV** would be hydrolyzed, presumably only the moiety corresponding to **V** is visible in data set #8, and the rest of the molecule is most likely disordered. In #10, which had been soaked in ethyl methylphosphonic acid (**VI**), the active site was occupied by polyacrylic acid, which was a component of the precipitant.

Table 9 also displays data for Apo-PTE_C23 crystal structures obtained from the MBP-PTE fusion constructs, one apo (#14), and five putative complexes (#12-13, #15-16, and #21), all six diffracting to 2.05 Å or better. In #12 and #13, SO_4^{-2} ions derived from the precipitant were observed in the active site, rather than the ligand soaked in. The sulfate ions are capable of chelating with the adjacent Zn^{+2}, as indeed can be seen upon examination of the crystal structures. In #15, electron density corresponding to the methyl phosphonate (**V**) soaked in can be clearly distinguished. In #16 and #21, electron density corresponding to **V** can similarly be clearly distinguished. Since the two ligands are not expected to be hydrolyzed, it is plausible, as in #8, that only the moiety corresponding to two negatively charged oxygens attached to the P atom, that

is tightly associated with the PTE is visible, and that the rest of the molecule, in both cases, is disordered.

Fig.10 shows the excellent fit of methyl phosphonate (**V**) into the electron density in data set #15.

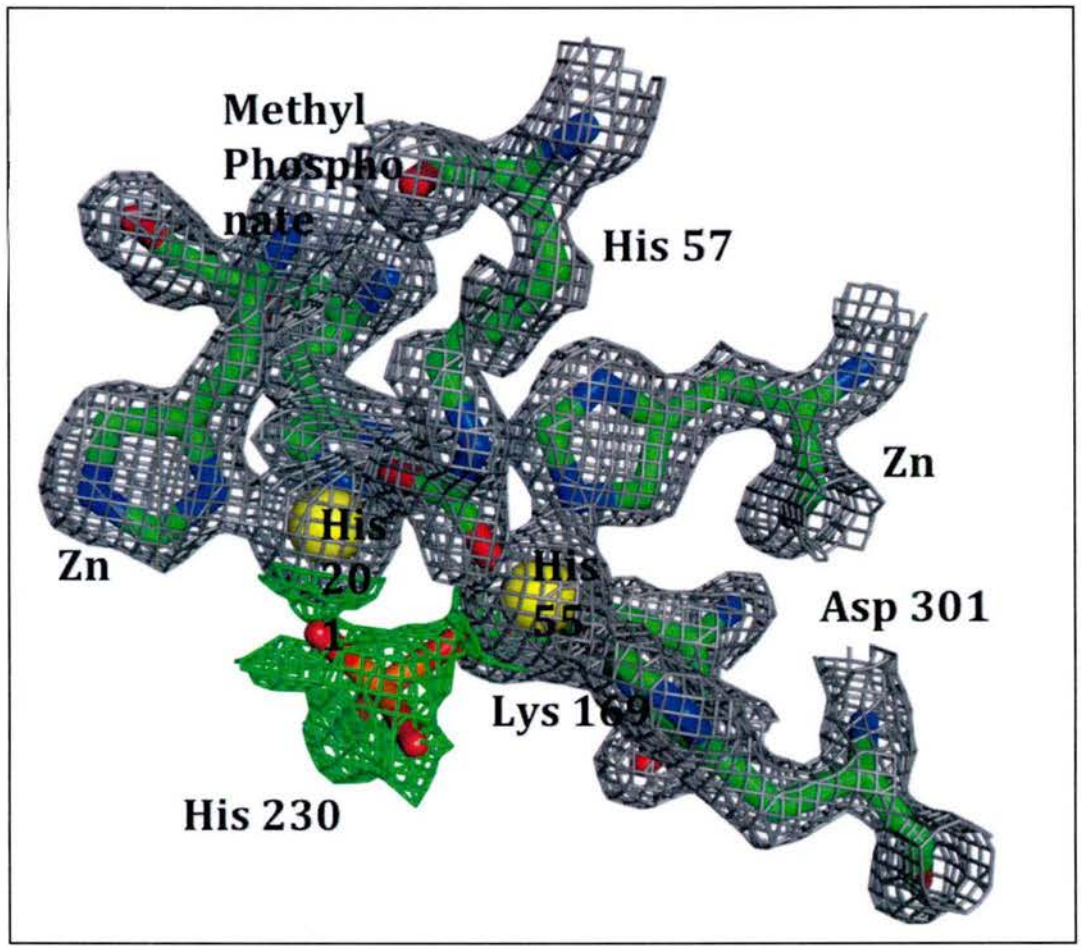

Figure 10: Electron density maps of the active-site region of the PTE_C23_PP structure exhibit electron density (green) corresponding to the methyl phosphonate (**V**). The 2Fo-Fc map contoured at 1 σ is shown in gray. The Fo-Fc map contoured at 2.5 σ shown in green.

Figs 11A and 11B display ligplots of the interactions made by methyl phosphonate (**V**) in its PTE_A53 (#9) and PTE_C23 (#15) complexes, respectively. In both cases, the ligplots highlight the interactions of the phosphonate moiety with the two Zn^{+2} ions, and with the same key amino acid residues within the active site, *viz.*, H55, W131, and H201, with other conserved residues, *viz.*, H57, H230, and D301, and with H55, as well as interacting with one or the other of the two Zn^{+2} ions

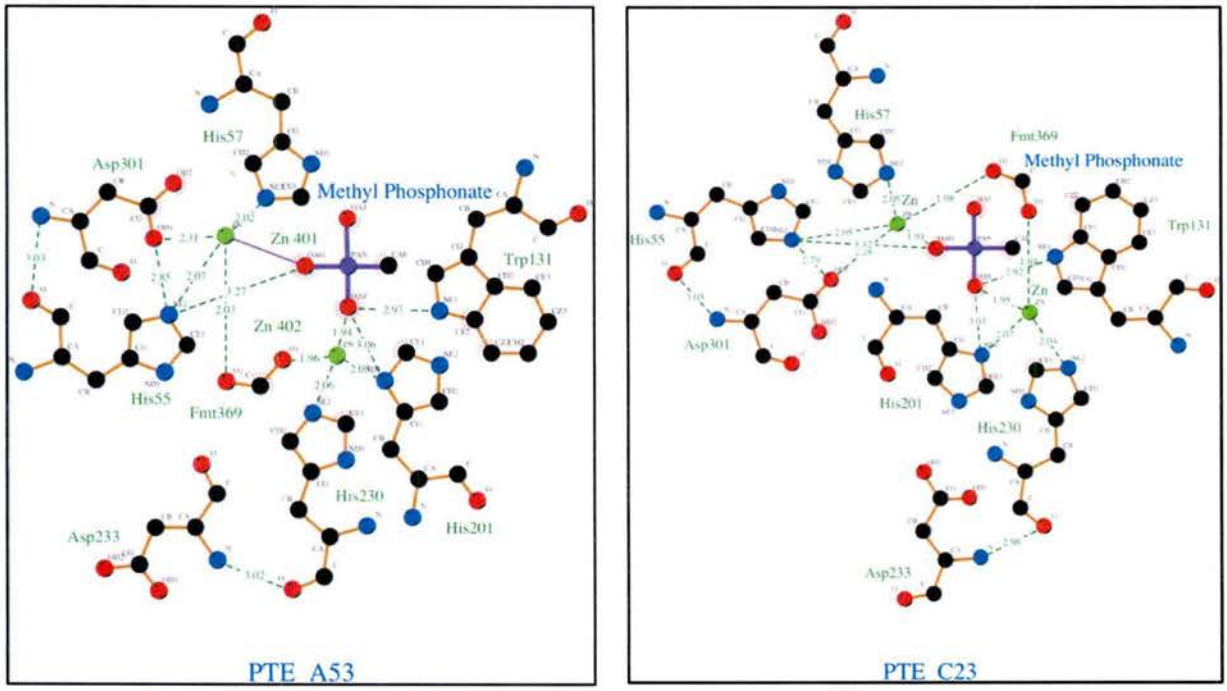

Figure 11: Schematic representation, using LigPlot (Wallace et al, 1995) that shows the interaction of methyl phosphonate (**V**) with (a) PTE_A53 (#9); (b) PTE_C23 (#15).

To summarize, OP ligands bearing two negatively charged oxygens capable of cross-bridging the two Zn^{2+} atoms (III, IV, V, and VI, Fig. 5) displayed electron density that could be fitted to the $CH_3P(=O)(O^-)$ moiety of the soaked $CH_3P(=O)(O^-)OR$ ligand, presumably due to the OR alkoxy chain being disordered.

It is of interest to point out that despite the extensive mutagenesis and evolution, the structure of the active site of the lead variant was maintained.

4.2.1 The N-termini of the cleaved A53 variants bear a peptide that penetrate their active sites

An interesting finding made upon close examination of the crystal structures described above, was that the N-terminal sequence of a crystallographically related molecule penetrates into the active site of one of the subunits of A53 (Figs. 11a and 11b) mimicking a peptide inhibitor. This observation is important since our earlier attempts to obtain crystals containing substrate analogs either by soaking or by co-crystallization had not met with much success. We were now able to obtain crystals of the PTE variants, C23, A53 and A203L with and without methyl phosphonate (Figs. 12, 13). Since the methyl phosphonate moiety represents only a small part of VX, the binding mode of most of it is, therefore, largely unknown. The N-terminal peptide seen within the active site of A53 is thus of great importance since it provide us with insights into the putative modes of binding of an inhibitor within the active site of A53.

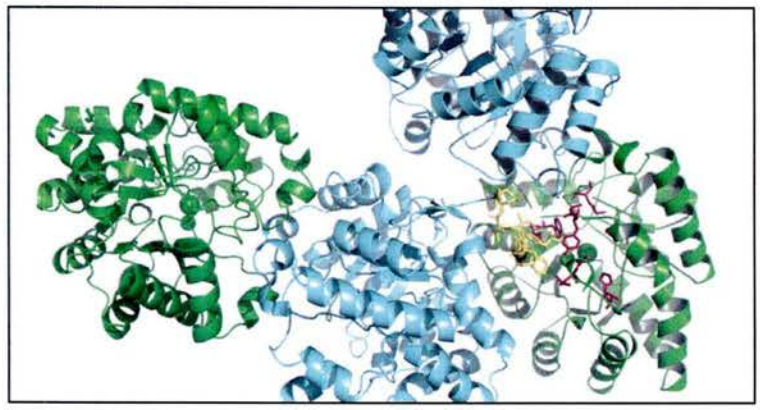

Fig. 12a

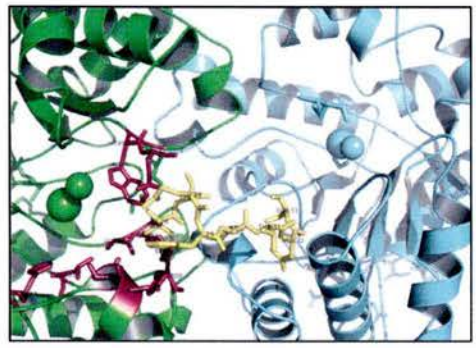

Fig. 12b

Figure 12: A diagram showing the N-terminusl of subunit B of A53 (yellow) protruding into the active site of subunit A (magenta) in a symmetry-related molecule. Subunits A and B are shown in green and cyan respectively. Fig. 12b: a closer view of Fig. 12a.

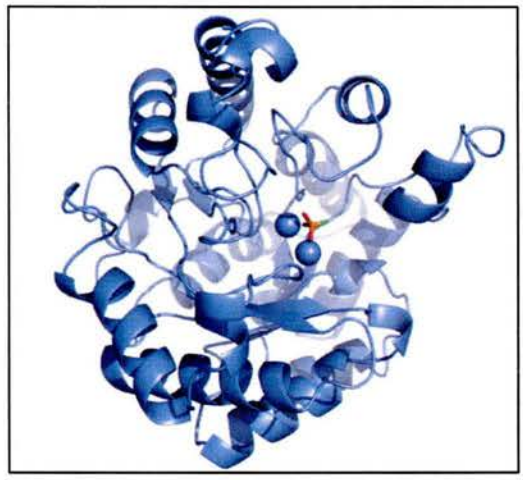

Figure 13: Cartoon representation showing the presence of methyl phosphonate in the active site of A53

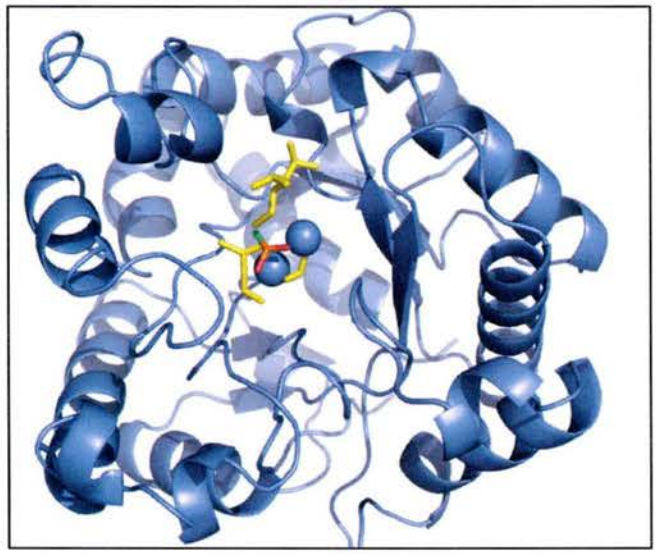

Figure 14: Alignment of the crystal structure of the complex of A53 with methyl phosphonate and of a computational model containing the transition state of a V-type nerve agent.

In an attempt to obtain better understanding of the mode of interaction of V-type nerve agents with PTE, we superimposed a computational model of PTE, containing the transition state of a V-type nerve agent, and the crystal structure of the complex of methyl phosphonate with A53. It shows that the binding mode predicted by the computational model resembles that in the crystal structure of the complex (Fig. 14).

4.2.2 Crystallization of C23-m2p0

Elucidation of the 3D structure of C23-m2p0 is of interest since it can highlight structural features that stabilize this variant. Over-expressed tagless C23-m2p0 yielded crystals using 12 % glycerol/1.5 M NH_4 $(SO_4)_2$/0.1 M Tris pH 7.5 as the precipitant (Fig. 15). A data set on one of these crystals, which diffracted to 2.3 Å, was collected 'in house', at the WIS X-ray Crystallography Facility. The data collected are summarized in Table 10.

Figure 15: The crystals of C23-m2p0

Table 10: Crystal data for PTE_C23_m2p0

	PTE_C23_m2p0
Unit cell axes (Å)	69.4, 69.4, 186.5
Unit cell angles (deg)	90, 90, 90
Space group	$P4_32_12$
Number of PTE chains in the asymmetric unit	1

The structures were determined by molecular replacement, using the native PTE_C23 crystal structure as the starting model. They were refined using CCP4/REFMAC5, and fitted into the electron density with COOT. The structure is in the final stages of refinement, and the interim crystallographic refinement statistics are shown in **Table 11**.

Table 11: Crystallographic refinement statistics for the PTE_C23_m2p0 crystal structure

	PTE_C23_m2p0
Resolution (Å)	2.3
Completeness (%)	100
R_{work} (%)	17.9
R_{free} (%)	21.3

4.3 Computational design of V-type hydrolyzing agents via engineering of bacterial PTE (sub-contracted work performed by the group of David Baker at U Washington)

4.3.1 Introduction and Background Information

The design of a prophylactic enzyme acting on nerve agents of the V-series has not yet been achieved. The objective of this project is to develop a new generation of PTE bioscavengers as prophylactic antidotes against chemical warfare nerve agents that are capable of enhanced degradation of V-type nerve agents. It was our goal to deliver two or more PTE enzyme variants that are both sufficiently potent and pharmaceutically suitable to provide prophylactic protection against V-series nerve agents at protein doses of ≤50 mg per 70 kg body weight, capable of hydrolyzing these toxins at k_{cat}/K_M >1x10^7 $M^{-1}min^{-1}$. In addition to the V-series nerve agents, G-series nerve agents, such as soman (GD) and cyclosarin (GF), also pose a significant threat. Therefore, we also aimed to expand the ability of our designed enzymes to hydrolyze

both types of toxic substrates, with the goal of developing a universal prophylactic enzyme.

The V-series nerve agents with larger chemical moieties at the *O*-ether position, RVX (*O*-isobutyl) and CVX (*O*-*n*-butyl), are not catalyzed as effectively by PTE as VX (*O*-ethyl) due to steric hindrance in the active site. At the start of our project, the most active PTE variant toward RVX and CVX, called "A53", had a mutation from leucine to alanine at position 106 (L106A), to permit accommodation of the bulkier VX moieties. Furthermore, it was observed in the initial rounds of directed evolution that second shell mutations behind residue 106 seemed to correlate with increased activity of A53 towards RVX and CVX (Cherny et al., 2013). Specifically, this was achieved by changing C59 to valine or phenylalanine (C59V or C59F). C59 residue is indeed in the second shell behind L106A, and presence of the bulkier Phe at this position enhanced the rate of RVX hydrolysis. Another PTE variant, C23, that bore a Y309W second-shell mutation, was found to have a preference for hydrolyzing the *S*p enantiomer of VX over the *S*p isomers of RVX and CVX.

Previous attempts to model VX agents in the PTE active site (in both the ground state and the transition state) illustrated the computational difficulties in docking substrates into catalytic metal sites. Nevertheless, with added geometrical restraints between the metal site and the substrate models, our preliminary docking studies correlated reasonably well with experimental observations for the catalytic preference for *S*p- and *R*p-isomers. These docking studies showed clear trends, *e.g.*, they indicated that presence of a smaller residue at position 106 should favor action on RVX and CVX. Taken together, these observations suggested that the active site of the A53 PTE variant could be remodeled, through secondary and tertiary shell mutations, for improved catalytic efficiency towards RVX, CVX, GD, and GF. To do this, it was clear from the outset that it would be necessary to understand the catalytic mechanism by correlating atomistic protein structure modeling data with experimental observations.

Our tasks were as follows:
(1) To refine the computational models for improved transition state alignment by adding experimental restraints extracted from both mutational and kinetic observations.
(2) To identify and remove destabilizing mutations from earlier computational PTE design libraries.
(3) To computationally investigate amino acid positions in PTE that could potentially increase the catalytic activity towards GD and GF such that the enzyme would reach the desired catalytic rate.

4.3.2 Methods

1. RosettaDock

Rosetta parameters were previously generated for the *S*p- and *R*p-isomers of VX, RVX, and CVX. The substrate models were inserted into the active site using the RosettaDock algorithm(Davis et al., 2009; Meiler and Baker, 2006). No geometrical restraints were made between the ligand and the metal site during docking, but all

poses were scored based on the distance between the phosphoryl oxygen and the ZnB atom. The top scoring poses were visually inspected and chosen for design and rigid body minimization.

2. Restraint Minimization of Ground and Transition State Models

A geometrical distance restraint of 2.15 +/- 0.25 Å, was added between ZnB and the phosphonyl oxygen, and rigid-body minimization was performed using Talaris2014 with RosettaScripts(Fleishman et al., 2011). To investigate the correlation between residue size at position 106 and the substrate, restraints were added between the Cα atom of position 106 (A/I) and the substrate models.

3. Sequence Analysis of Computer and Experiment Guided Designs

The sequences of the latest computational and experimental guided designs were aligned using the muscle algorithm(Edgar, 2004), and designed positions were scored using a position-specific scoring matrix (PSSM) based on psipred (McGuffin et al., 2000).

4. ddG computation of Computer and Experiment Guided Designs.

The ddG was computed for each of the designed substitutions using the ddG monomer application in Rosetta with default settings. This allows us to assess the structural changes and energetic re-stabilizing or de-stabilizing effects of each substitution in PTE.

5. Generation of transition state models of GD and GF

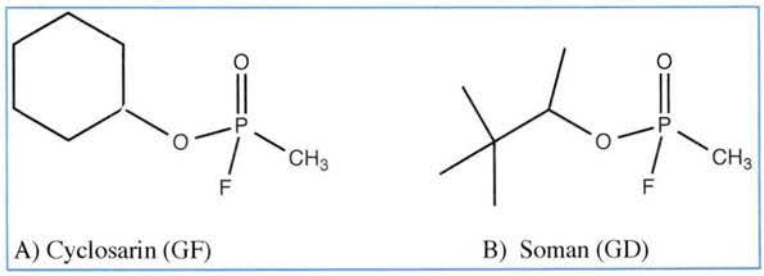

Figure 16. Nerve agents of the G-series. (A) Cyclosarin with the bulky *O*-hexyl moiety. B) Soman with the branched *O*-pinacolyl moiety.

The structures of GD and GF (Fig, 16), were modeled into the active site of PTE; the *S*p-isomer of GF and the *SpSc* isomer of GD were used, since they are the more toxic isomers of the racemic G nerve agents (Goldsmith et al., 2012). Notably, the racemic mixture of soman contains two pairs of diastereisomers and 2 of the 4 optical isomers are toxic. Here we modeled one of the toxic isomers, *SpSc*. Transition state (TS) models of the compounds were generated by placing a hydroxide for in-line attack on the phosphorus atom, with a distance of 1.7 Å between the phosphorus atom and

the oxygen atom of the hydroxide. The distance of the bond breaking of the P-F bond was set to 2.44 Å as observed from quantum mechanical calculations(Dyguda-Kazimierowicz et al., 2008). Lastly, conformers were generated for both of the models using Babel, and all conformers were evaluated visually using PyMOL(http://www.pymol.org).

6. Docking of GD and GF into PTE

The TS models were docked into the crystal structure of the three PTE variants, A53, C23, and C23_A203L, using RosettaDock(Meiler and Baker, 2006). Restraints were added during docking in order to sample efficiently around productive states by adding a distance restraint of 3.0 Å +/- 0.5 between the phosphonyl oxygen and ZnB, and a distance restraint of 3.0 Å between the hydroxide oxygen and ZnA. Five thousand poses were generated and sorted by lowest interface energy and restraint score.

7. Design of structure

To improve the enzymes, we used the RosettaDesign algorithm(Kuhlman et al., 2003) to optimize the interactions between the protein and the TS models. Furthermore, we added in mutations that have been observed to increase the catalytic rate of G-series nerve agent decomposition: L303AT, H257Y, H254G.

4.3.3 Results

1. Docking of nerve agents into PTE variants

To better understand the mutations observed during directed evolution, models of two enantiomers of the VX isomers were docked into the active site of three PTE variants, *viz.*, A53, C23, and C23_A203L. To understand the placement of the substrate, different models were generated to mimic both the ground states as well as the transition states; docking of transition states can give better agreement with experimental results.

The docking poses were filtered based on the distance between the phosphonyl oxygen and ZnB, since this zinc ion functions as an oxyanion hole during hydrolysis of the nerve agent, as well as on the distance between the oxygen of the hydroxide and the phosphorus atom distal to the leaving group.

First, we analyzed the docked poses to investigate if any immediate trends were observed. In the case of the *Sp* isomer in the V-series, a trend was observed with respect to position 106, which showed that larger active-site residues have preference for substrates with smaller side-groups. This observation agrees with computation models and kinetic measurements that showed that a decrease in the size of the side chain at position 106 (A and V) increases the catalytic hydrolysis rate of RVX, and larger amino acids at 106 (I and L) are optimal for hydrolysis of VX. Another space-

filling mutation is L271F, which increases the catalytic efficiency for VX but decreases that for *Sp*-RVX. Interestingly, A203 mutated to L increases the catalytic efficiency, but no epistasis is observed when it is combined with I106A or I106L, or combined with L271F for VX or RVX.

We hypothesized that mutations at position 257 should have the opposite effect on the stereoselectivity, with bulkier groups being less efficient when combined with I106, but an increase in catalytic efficiency was observed when this position was combined with A203.

The docked poses of *Sp*-VX in the ground state of the molecule capture the charge-charge interaction between E132 and the N-tertiary amine of the leaving group. It was observed in the docked poses that the carboxyl group of E132 was close to the sulfur atom, suggesting it might have also a polarizing effect either on the sulfur itself or mediated through a water molecule. In some of the poses the *O*-ethyl is in van der Waals contact with I106 as well as with L303. W131 may contribute to the oxyanion hole by hydrogen bonding to the phosphonyl oxygen.

2. Investigation of second shell mutations around position106

To improve the models of the ground and transition states, a rigid body minimization was performed between the phosphonyl oxygen and ZnB of PTE. This was performed to compensate for the polarization effects of the metal site, which cannot be captured by a simple classical force field model. A distance restraint of 2.15 Å was applied based on statistics from the PDB(Harding and Hsin, 2014), and the complex was minimized.

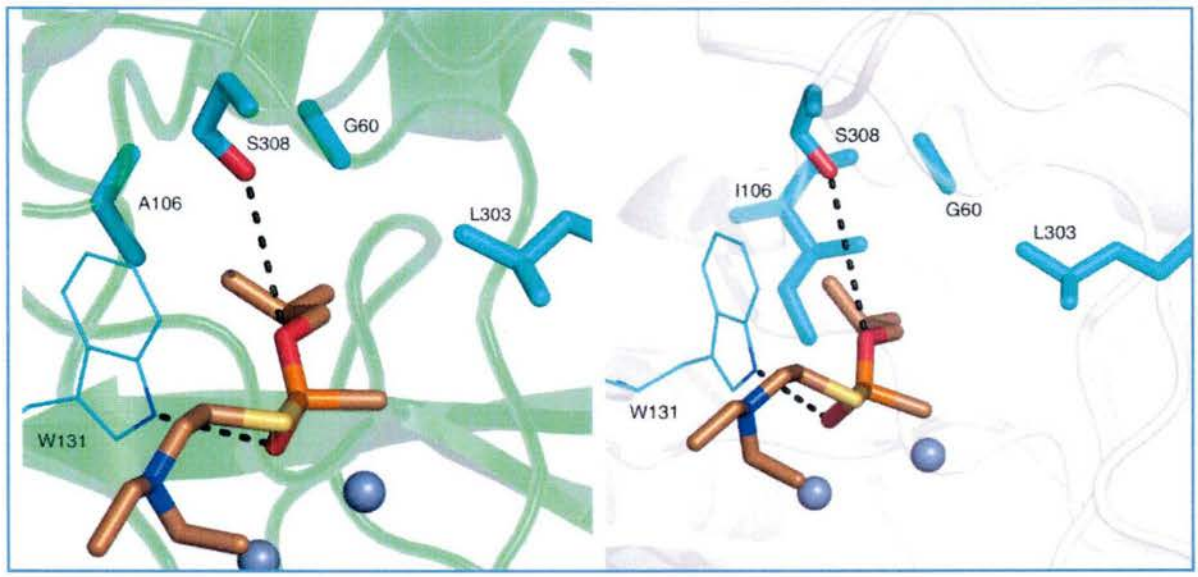

Figure 17. Binding pocket for *O*-isobutyl. (Left) Shown are the main residues in variant A53 that form the pocket which accommodates the *O*-isobutyl of RVX. Here, the wild type residue I106 has been substituted by an Ala residue. (Right) Substitution of Ala back to the native residue Ile decreases the size of the binding pocket and creates steric clash with the substrate.

Fig. 17 shows how the isobutyl group of RVX approaches position 106. According to the computational models, to create more room for bulkier side groups of the V-series it is necessary to mutate residues in the second shell adjacent to position 106, such as A63, F104, and D105, to increase/decrease the volume (Fig. 18). These three residues have high connectivity to other residues within the protein, and are close to the interface between the two monomers where mutations have been hard to incorporate. Firstly, the conservation of the residues was investigated computing a PSSM for the native protein from *Pseudomonas diminuta*. A63 and D105 display little variance, with only Ser at position 63 scoring higher than native. For position 105 only a Gly is observed in the PSSM, whereas for F104 many more possibilities are possible (see Table 12). The $\Delta\Delta G$ calculations for F104A and D105A substitutions showed that D105A has a favorable energy (-2.325 REU), whereas F104 has a disfavorable energy (2.599 REU). These results suggest a minimal library at the following three positions: A63S, F104IV, and D105G.

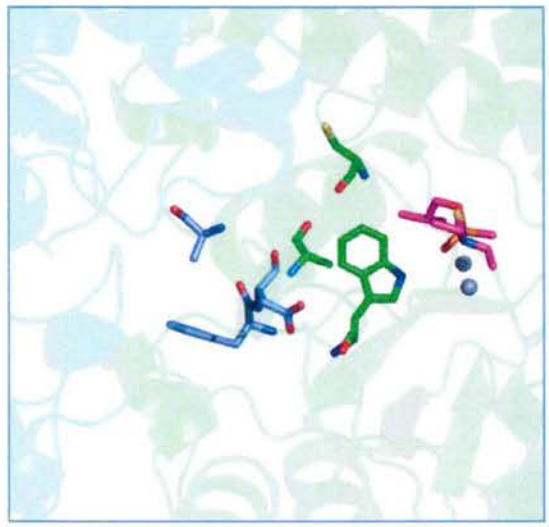

Figure 18. The second shell residues in "A53": A63, F104, and D105 (purple sticks) confine the loop which supports position 106. Also shown are the two zinc ions (grey spheres), W131 (green sticks), A106 (green sticks), C59 (green sticks) and Rp-VX (magenta).

After refinement of the docking models, we observed that W131 both packs with the side group of the *S*p-VX isomer and donates a hydrogen bond to the phosphonyl oxygen, suggesting a role as part of the oxyanion hole during the chemical reaction. This could explain the fact that any attempt to mutate this position has resulted in reduced activity. Furthermore, the role of E132, which is a designed residue, could be to polarize the sulfur atom of the leaving group through a water molecule.

3. Analysis of Conservation Score from Focus Library

The PTE enzyme library was constructed from residues computationally predicted to increase nerve agent catalysis in PTE, with the goal of combining multiple mutations to achieve additive effects. To reduce the chances of destabilizing the PTE with too many mutations at once, only a few new residues were added to the library that had not previously been validated as being compatible with overall PTE structure (Table

13). The F132TI substitutions were considered risky, since F132E has converged in PTE towards the hydrolysis of the V-series. Nevertheless, these mutations were included, since they have been found in other VX hydrolysis assays(Tsai et al., 2012) , but are new in our testing

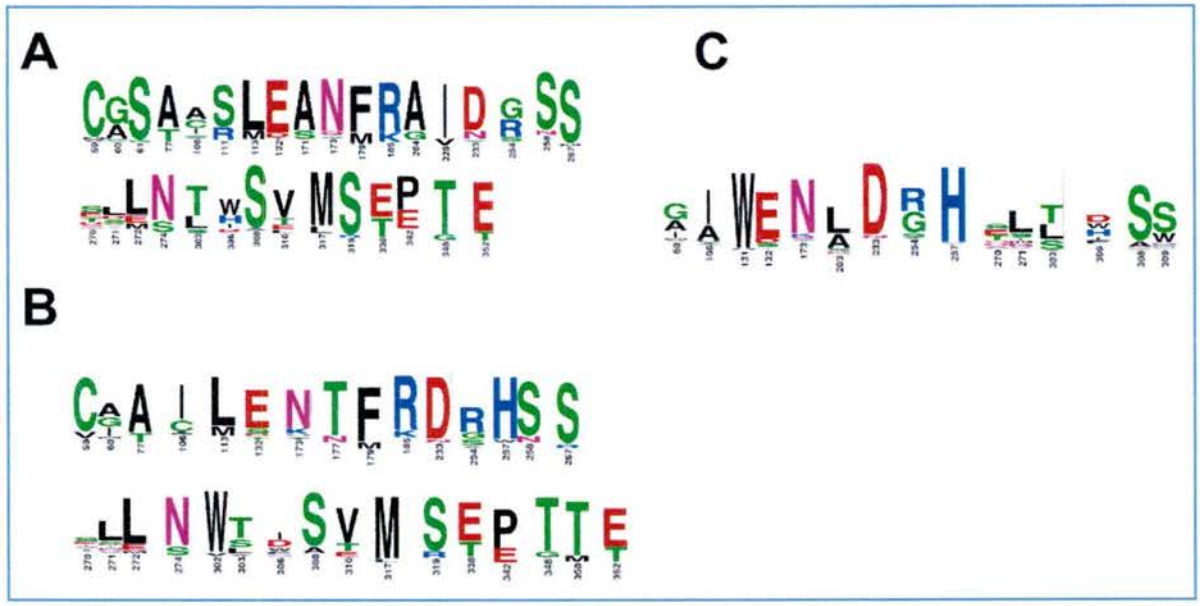

Figure 19. Logo plot of design sequences in focus library. (A) and (B) show the positions and amino acids entities for the focus library based on the ground state and transition state models respectively, where only previous mutations were allowed to be incorporated into the protein. (C) shows the designed positions and which amino acids were allowed to be incorporated. In this set, previously observed mutations were given a bonus while new amino acids were allowed into the design.

The average number of mutations compared with the stabilized variant for *Sp*-VX, C23-m2p0-Y309W, was 10 (+/- 6) and the median was 8, where 14 contained more than 10 mutations. Fig. 19 shows a logo plot with the distribution of amino acids and which positions had been changed.

Table 12: Position Specific Score Matrix for A63, F104, and D105

pos/ AA	A	R	N	D	C	Q	E	G	H	I	L	K	M	F	P	S	T	W	Y	V
A63	12	1	1	7	0	1	7	9	0	8	8	3	3	1	6	17	7	0	2	6
F104	8	9	3	1	0	1	3	5	4	10	5	4	3	2	8	3	8	0	9	15
D105	0	0	5	19	0	0	3	55	0	0	0	0	0	2	0	6	0	0	11	0

Table 13: Computational Design Library for G-series nerve agents

Position	Native Amino Acid	New
60	G	M,I
132	F	T,I
136	L	M,L,G,Q
306	F	D,S

4.3.4 Discussion

Improved alignment of the transition state models was performed using RosettaDock followed by minimization. It was observed that it was necessary to minimize the docked poses using restraints to get the oxygen of the phosphonyl close to the Zn^{+2} ion. With this minimization it was further observed that I106 would present a steric challenge for the TS models to get closer to the Zn^{+2}. This is in agreement with the mutational data for the bulkier fragments, which have lower activity compared with *Sp*-VX.

Given the alignment of the TS models, we computationally redesigned the second shell residues around A106. We observed that the second shell residue C59 was enriched during directed evolution. The first shell residues are highly connected to the metal site, making it problematic to introduce mutations in this area. This made it necessary to engineer the second and third shell mutations to introduce the necessary flexibility to accommodate the bigger chemical fragments of RVX and CVX. Besides

computing the $\Delta\Delta G$ values of the potential residues, we also cross-validated the potential mutations with their evolutionary score to optimize their success of incorporation.

The interactions with the TS models of cyclosarin and soman were optimized using the RosettaDesign algorithm. E132 was changed during the design, which has shown to be important for the catalysis of V-agents due to its potential interaction with the tertiary amine of the N-alkyl. This chemical group is replaced by a fluoride in the G-series and from the RosettaDesign it is designed to a T or I. The other positions were mainly to increase the interactions to the TS models.

5. Non-funded collaborations:

5.1 The group of Prof. Franz Worek (Bundeswehr Institute of Pharmacology & Toxicology, Munich)

The tagless C23-A203L variant was purified and delivered to Prof. Franz Worek at the Bundeswehr Institute of Pharmacology & Toxicology (Munich, Germany) to be tested against s.c. VX intoxication by employing the previously published protocol for the evaluation of MBP-tagged C23 in guinea pigs (Worek et al., 2014). The present study demonstrated for the first time the suitability of intraosseous (i.o) injection of a PTE in nerve-agent-poisoned guinea pigs. This mode of injection resulted in PTE plasma levels comparable to those achieved by i.v. administration and in similar therapeutic efficacy. I.o. vascular access systems may allow a safe and rapid route for administration of a catalytic bioscavenger to the systemic circulation, and could improve post-exposure PTE therapy of nerve agent poisoning. (Manuscript submitted to Toxicology Letters).

5.2 The group of Dr. Sarel Fleishman (Dept. of Biomolecular Sciences, Weizmann Institute).

In order to increase the stability of our evolved PTE variants we collaborated with the group of Dr. Sarel Fleishman, which specializes in computational design. Adi Goldenzweig, a Ph.D. student in his lab, developed and employed a novel algorithm to analyze the evolved PTE variant C23, and provided a list of residue substitutions that could increase its thermodynamic stability. We ordered the synthesis of three stabilized designs of variant C23 based on the output of the algorithm, and tested them for thermostability and metal-binding affinity. Two of the three designs provided variants that were more thermostable and had better metal binding affinity than the original C23 variant. Using the best design, we were able to continue and introduce novel mutations into C23, and to obtain PTE variants with higher catalytic efficiency while maintaining stability. The description of this effort will also be included in a manuscript that is in preparation.

6. Future Plans

Pending budget availability from DTRA, we submitted a detailed proposal aimed at the following goals: To develop clinically applicable catalytic bioscavengers that can efficiently hydrolyze all G- and V-type threat nerve agents with high catalytic efficiencies ($k_{cat}/K_M \geq 10^7$ $M^{-1}min^{-1}$), thus providing effective long-term protection, reduced mortality and alleviated morbidity, following nerve agent intoxication. Specifically, to develop catalytic bioscavengers for broad-spectrum nerve agent prophylaxis based on our previously engineered PTE variants, C23 and A53, with the required *in-vivo* efficacies, pharmacokinetic, immunogenic and safety profiles, and to acquire preclinical data that will support their future Target Product Profile.

We proposed the following milestones:

1) Engineering and evolution of variants with catalytic proficiencies of k_{cat}/K_M $\geq 1x10^7$ $M^{-1}min^{-1}$(optimally $5x10^7M^{-1}min^{-1}$) when reacting with G- and V-type nerve agents.
2) Performance of pharmacokinetic (PK) studies in order to: (a) determine mean residence time (MRT) of the PTEs; (b) determine time to peak in plasma and the terminal half-life, so as to set an optimal time for administration of PTEs to achieve the best protection; (c) evaluate protein modification so as to enhance circulatory life time.
3) Determination of protection efficacy of PTE variants in mice and rats challenged with broad-spectrum OP nerve agents.
4) Engineering of selected promising enzyme variants so as to improve their bio-pharmaceutical properties, including increased storage and *in vivo* life spans, and reduction of immunogenicity.
5) Performance of safety profiles on selected engineered variants.
6) Study of combinations of variants so as to cover the broad spectrum of G and V-type nerve agents. This will include protection efficacy and PK characteristics.
7) Performance of whole body exposure to GB and VX of animals pre-treated with the most promising variant combinations.
8) Determination of the cross-reactivity of most promising combination with current therapeutics, using atropine, 2-PAM and diazepam, both *in vitro* and *in vivo.*
9) Optimize over-expression in bacteria and subsequent purification of the most promising variant candidates.

Decision points along the trajectory of project development will be based on go/no-go key criteria to be set specifically for each Task.

7. Publications and Technical reports (during 4th option year)

7.1 Two technical quarterly reports were submitted to DTRA, which covered the 1st, 2nd quarters of the 4th option year.

7.2 Catalytic efficiencies of directly evolved phosphotriesterase variants with structurally different organophosphorus compounds in vitro.

Goldsmith M, Eckstein S, Ashani Y, Greisen P Jr, Leader H, Sussman JL, Aggarwal N, Ovchinnikov S, Tawfik DS, Baker D, Thiermann H, Worek F. Arch Toxicol. 2015 Nov 26. [Epub ahead of print]

7.3 In vitro evaluation of the catalytic activity of paraoxonases and phosphotriesterases predicts the enzyme circulatory levels required for in vivo protection against organophosphate intoxications, Ashani Y, Leader H, Aggarwal N, Silman I, Worek F, Sussman JL, Goldsmith M., Chem Biol Interact. 2016 May 6. pii: S0009-2797(16)30175-2. doi: 10.1016/j.cbi.2016.04.039. [Epub ahead of print]

7.4 An unfunded collaboration with Prof. F. Worek (Munich) resulted in a manuscript (in preparation) entitled: Single treatment of VX poisoned guinea pigs with the phosphotriesterase mutant C23-A203L: Intraosseous versus intravenous injection

7.5 Presentations: Drs Goldsmith and Ashani presented parts of the results discussed above at the 12th ChE-PON6 meeting, Elche-Alicante, Spain, Sep 2015.

8. References

Afriat-Jurno L et al., 2012, Reconstructing a missing link in the evolution of a recently diverged phosphotriesterase by active-site loop remodeling, *Biochemistry*, 51, 6047-6055.

Ashani Y and Pistinner S, 2004, Estimation of the upper limit of human butyrylcholinesterase dose required for protection against organophosphates toxicity: a mathematically based toxicokinetic model. *Toxicol Sci*, 77, 358-367.

Ashani Y et al, 2016, In vitro evaluation of the catalytic activity of paraoxonases and phosphotriesterases predicts the enzyme circulatory levels required for in vivo protection against organophosphate intoxications. *Chem-Biol Interaction*, available online, May 2016.

Ben-David M *et al*, 2013, Catalytic metal ion rearrangements underline promiscuity and evolvability of a metalloenzyme. *J Mol Biol*, 425, 1028-1038.

Berman HA & Leonard K, 1989, Chiral reactions of acetylcholinesterase probed with enantiomeric methylphosphonothioates. Noncovalent determinants of enzyme chirality *J Mol Biol*, 264, 3942-3950.

Bird SB et al, 2008, OpdA, a bacterial organophosphorus hydrolase, prevents lethality in rats after poisoning with highly toxic organophosphorus pesticides. *Toxicology*, 247, 88-92.

Cherny I *et al*, 2013, Engineering V-type nerve agents detoxifying enzymes using computationally focused libraries. *ACS chemical biology,* **8**, 2394-2403

Davis IW, and D. Baker, 2009, RosettaLigand docking with full ligand and receptor flexibility. *Journal of molecular biology,* **385**, 381-392.

Dyguda-Kazimierowicz E, Sokalski WA, Leszczynski L, 2008, Gas-phase mechanisms of degradation of hazardous organophosphorus compounds: do they follow a common pattern of alkaline hydrolysis reaction as in phosphotriesterase? *J Phys Chem B,* **112**, 9982-9991 .

Edgar RC, 2004, MUSCLE: multiple sequence alignment with high accuracy and high throughput. *Nucleic acids research,* **32**, 1792-1797.

Fleishman SJ *et al.*, 2011, RosettaScripts: a scripting language interface to the Rosetta macromolecular modeling suite. *PloS one* , **6**, e20161.

Gersham C et al, 2010, Kinetics and efficacy of an organophosphorus hydrolase in a rodent model of methyl-parathion poisoning. *Acad. Emerg. Med.* 17, 736-740.

Goldsmith M *et al*, 2012, Evolved stereoselective hydrolases for broad-spectrum G-type nerve agent detoxification. *Chem Biol* , **19**, 456-466 .

Goldsmith M et al, 2015, Catalytic efficiencies of directly evolved phosphotriesterase variants with structurally different organophosphorus compounds in vitro. *Arch. Toxicol*, November 2015 (Epub ahead of print)

Gupta RD *et al*, 2011, Directed evolution of hydrolases for prevention of G-type nerve agent intoxication. *Nat Chem Biol*, 7, 120-125.

Harding MM, and Hsin KY, 2014, Mespeus--a database of metal interactions with proteins. *Methods Mol Biol* . **1091**, 333-342 .

Jackson CJ et al, 2014, Use of OpdA, an organophosphorus (OP) hydrolase, prevents lethality in an African green monkey model of acute OP poisoning. *Toxicology*, 317, 1-5.

Khare SD *et al*, 2012, Computational redesign of a mononuclear zinc metalloenzyme for organophosphate hydrolysis. *Nat Chem Biol,* 8, 294-300.

Kuhlman B, *et al.*, 2003, Design of a novel globular protein fold with atomic-level accuracy. *Science* **302**, 1364-1368 .

McGuffin LJ, Bryson K, and Jones DT, 2000, The PSIPRED protein structure prediction server. *Bioinformatics* **16**, 404-405.

Meiler J and D. Baker, ROSETTALIGAND, 2006, protein-small molecule docking with full side-chain flexibility. *Proteins* **65**, 538-548.

Tsai PC et al., 2012, Enzymes for the homeland defense: optimizing phosphotriesterase for the hydrolysis of organophosphate nerve agents. *Biochemistry* **51**, 6463-6475.

Wallace AC, Laskowski RA, Thornton JM 1995 LIGPLOT: a program to generate schematic diagrams of protein-ligand interactions. *Protein Eng* 8, 127-134.

Worek F et al., 2014, Post-exposure treatment of VX poisoned guinea pigs with the engineered phosphotriesterase mutant C23: a proof-of-concept study. *Toxicol. Lett.* 18, 45-54

Worek F et al, 2016, Single treatment of VX poisoned guinea pigs with the phosphotriesterase mutant C23AL: Intraosseous versus intravenous injection *Toxicol. Lett*, submitted

9. Appendix – Amended Publications and Technical Reports

Technical reports- 15 quarterly reports and 5 annual reports throughout the entire contract period

Publications (for the entire contract period):

Automated Structure- and Sequence-Based Design of Proteins for High Bacterial Expression and Stability. Goldenzweig A, Goldsmith M, Hill SE, Gertman O, Laurino P, Ashani Y, Dym O, Unger T, Albeck S, Prilusky J, Lieberman RL, Aharoni A, Silman I, Sussman JL, Tawfik DS, Fleishman SJ.
Mol Cell. 2016 Jul 21;63(2):337-46. doi: 10.1016/j.molcel.2016.06.012. Epub 2016 Jul 14.

In vitro evaluation of the catalytic activity of paraoxonases and phosphotriesterases predicts the enzyme circulatory levels required for in vivo protection against organophosphate intoxications. Ashani Y, Leader H, Aggarwal N, Silman I, Worek F, Sussman JL, Goldsmith M.
Chem Biol Interact. 2016 May 6. pii: S0009-2797(16)30175-2. doi: 10.1016/j.cbi.2016.04.039. [Epub ahead of print]

Catalytic stimulation by restrained active-site floppiness--the case of high density lipoprotein-bound serum paraoxonase-1. Ben-David M, Sussman JL, Maxwell CI, Szeler K, Kamerlin SC, Tawfik DS.
J Mol Biol. 2015 Mar 27;427(6 Pt B):1359-74. doi: 10.1016/j.jmb.2015.01.013. Epub 2015 Jan 30.

Generating targeted libraries by the combinatorial incorporation of synthetic oligonucleotides during gene shuffling (ISOR).Rockah-Shmuel L, Tawfik DS, Goldsmith M. Methods Mol Biol. 2014;1179:129-37. doi: 10.1007/978-1-4939-1053-3_8.

Engineering V-type nerve agents detoxifying enzymes using computationally focused libraries. Cherny I, Greisen P Jr, Ashani Y, Khare SD, Oberdorfer G, Leader H, Baker D, Tawfik DS. ACS Chem Biol. 2013 Nov 15;8(11):2394-403. doi: 10.1021/cb4004892. Epub 2013 Oct 4.

Catalytic metal ion rearrangements underline promiscuity and evolvability of a metalloenzyme. Ben-David M, Wieczorek G, Elias M, Silman I, Sussman JL, Tawfik DS. J Mol Biol. 2013 Mar 25;425(6):1028-38. doi: 10.1016/j.jmb.2013.01.009. Epub 2013 Jan 11.

Evolved stereoselective hydrolases for broad-spectrum G-type nerve agent detoxification. Goldsmith M, Ashani Y, Simo Y, Ben-David M, Leader H, Silman

I, Sussman JL, Tawfik DS. Chem Biol. 2012 Apr 20;19(4):456-66. doi: 10.1016/j.chembiol.2012.01.017.

Catalytic versatility and backups in enzyme active sites: the case of serum paraoxonase 1. Ben-David M, Elias M, Filippi JJ, Duñach E, Silman I, Sussman JL, Tawfik DS. J Mol Biol. 2012 May 4;418(3-4):181-96. doi: 10.1016/j.jmb.2012.02.042. Epub 2012 Mar 1.

Computational redesign of a mononuclear zinc metalloenzyme for organophosphate hydrolysis. Khare SD, Kipnis Y, Greisen P Jr, Takeuchi R, Ashani Y, Goldsmith M, Song Y, Gallaher JL, Silman I, Leader H, Sussman JL, Stoddard BL, Tawfik DS, Baker D. Nat Chem Biol. 2012 Feb 5;8(3):294-300. doi: 10.1038/nchembio.777

Directed enzyme evolution: beyond the low-hanging fruit. Goldsmith M, Tawfik DS. Curr Opin Struct Biol. 2012 Aug;22(4):406-12. doi: 10.1016/j.sbi.2012.03.010. Epub 2012 May 12. Review.

Computational redesign of a mononuclear zinc metalloenzyme for organophosphate hydrolysis. Khare SD, Kipnis Y, Greisen P Jr, Takeuchi R, Ashani Y, Goldsmith M, Song Y, Gallaher JL, Silman I, Leader H, Sussman JL, Stoddard BL, Tawfik DS, Baker D. Nat Chem Biol. 2012 Feb 5;8(3):294-300. doi: 10.1038/nchembio.777.

Unfunded collaboration with Prof. Worek lab (in vitro and In vivo experiments, Munich Germany) using variants engineered expressed purified and studied at WIS under a DTRA project contract(HDTRA1-11-C-0026).

Single treatment of VX poisoned guinea pigs with the phosphotriesterase mutant C23AL: Intraosseous versus intravenous injection.
Wille T, Neumaier K, Koller M, Ehinger C, Aggarwal N, Ashani Y, Goldsmith M,Sussman JL, Tawfik DS, Thiermann H, Worek F.
Toxicol Lett. 2016 Sep 6;258:198-206. doi: 10.1016/j.toxlet.2016.07.004. Epub 2016 Jul 7.

Catalytic efficiencies of directly evolved phosphotriesterase variants with structurally different organophosphorus compounds in vitro.
Goldsmith M, Eckstein S, Ashani Y, Greisen P Jr, Leader H, Sussman JL, Aggarwal N, Ovchinnikov S, Tawfik DS, Baker D, Thiermann H, Worek F.
Arch Toxicol. 2015 Nov 26. [Epub ahead of print]

Post-exposure treatment of VX poisoned guinea pigs with the engineered phosphotriesterase mutant C23: a proof-of-concept study.

Worek F, Seeger T, Reiter G, Goldsmith M, Ashani Y, Leader H, Sussman JL, Aggarwal N, Thiermann H, Tawfik DS.
Toxicol Lett. 2014 Nov 18;231(1):45-54. doi: 10.1016/j.toxlet.2014.09.003. Epub 2014 Sep 6.

Presentations

1. 12th International Meeting of Cholinesterases and 6th paraoxonase Conference, 27-Sept-2 Oct 2015, Alicante, Spain; "In vitro evaluation of the catalytic activity of PONs and PTEs predicts the enzyme dose required for *in vivo* protection against organophosphate intoxication: verification of a concept."; Y. Ashani, M.Goldsmith, F. Worek, H.Leader, N, Agrawal, I, Silman, J.L. Sussman, D.S. Tawfik.- (Presenting Author: Yacov Ashani).

2. Enzyme Engineering XXIII conference, Sept 6-11, 2015, St. Petersburg, Florida, USA, The 2015 Enzyme Engineering Award was awarded to Professor Dan S. Tawfik.